January 2013

High-pressure cryogelation of nanosilica and surface properties of cryosilicas

V M. Gun'ko
Chuiko Institute of Surface Chemistry

V V. Turov
Chuiko Institute of Surface Chemistry

V I. Zarko
Chuiko Institute of Surface Chemistry

G P. Prykhod'ko
Chuiko Institute of Surface Chemistry

O S. Remez
Chuiko Institute of Surface Chemistry

See next page for additional authors

Authors
V M. Gun'ko, V V. Turov, V I. Zarko, G P. Prykhod'ko, O S. Remez, R Leboda, J Skubiszewska-Zieba, E M. Pahklov, and Jonathan Blitz

High-pressure cryogelation of nanosilica and surface properties of cryosilicas

V.M. Gun'ko,[a,*] V.V. Turov,[a] V.I. Zarko,[a] E.M. Pakhlov,[a] G.P. Prykhod'ko,[a]
O.S. Remez,[a] R. Leboda,[b] J. Skubiszewska-Zięba,[b] J.P. Blitz[c]

[a] *Chuiko Institute of Surface Chemistry, 17 General Naumov Street, 03164 Kyiv, Ukraine*
[b] *Faculty of Chemistry, Maria Curie-Skłodowska University, 20-031 Lublin, Poland*
[c] *Eastern Illinois University, Department of Chemistry, Charleston, IL 61920 USA*

Abstract

Silica cryogels (cryosilicas) in a powder state were synthesized with different concentrations of fumed silica A-300 ($C_{A\text{-}300}$ = 5-20 wt.%), sonicated in aqueous suspension, then frozen at −14 °C at different pressures in a high-pressure stainless steel reactor (a freezing bomb), and dried in air at room temperature. To analyze the effects of low temperature and high pressure, samples were also prepared at −14 °C or room temperature and standard pressure. The structural and adsorption properties of the powder materials were studied using nitrogen adsorption, high-resolution transmission electron microscopy, infrared spectroscopy, thermogravimetry, low-temperature ^{1}H NMR spectroscopy and thermally stimulated depolarization current. The structural, textural, adsorption and relaxation characteristics of high-pressure cryogel hydrogels and related dried powders are strongly dependent on the silica content in aqueous suspensions frozen at 1, 450 or 1000 atmospheres and then dried. The largest changes are found with $C_{A\text{-}300}$ = 20 wt.% which are analyzed with respect to the interfacial behavior of nonpolar, weakly polar and polar adsorbates using low temperature ^{1}H NMR spectroscopy.

Keywords: Nanosilica powder; High-pressure cryogelation; Interfacial phenomena; Bound water; NMR cryoporometry; Dispersion medium effects

∗ Corresponding author. Tel.: +38044 4229627; fax: +38044 4243567.
E-mail address: vlad_gunko@ukr.net (V.M. Gun'ko).

1. Introduction

Cryogelation, used to synthesize soft (polymer) or solid (oxides, carbons) cryogels at temperatures below a bulk solvent's (typically water) freezing point, allows the production of micro/macroporous materials from different organic or inorganic precursors [1-5]. Results of cryogelation of polymeric or solid matters strongly differ from that of freeze-drying. In the case of cryogelation, cryoconcentration of a solution or a suspension occurs in the liquid layers located between ice crystallites (porogens) and chemical (with a cross-linker reacting with a gel precursor) or physical (by intermolecular bonding of polymers or particles) cross-linking of macromolecules or nanoparticles occurs there. Freeze-drying with sublimation of a frozen solvent does not practically result in cross-linking of particles or macromolecules. In other words, cryogelation results in strong reorganization of solutes but freeze-drying should remain undamaged texture of the materials. Cryogels can be synthesized with varying textural, structural and adsorption characteristics. Typically, cryogels are macroporous materials with a great porosity and main pore sizes in the micrometer range (1-300 μm) [1-5].

Some examples of reported cryogel syntheses include solid cryogels based on oxide, carbon or hybrid precursors [1-5]. Porous titania cryogel fibers have been synthesized using unidirectional freezing and subsequent freeze-drying of titania hydrogels. The hydrogels were synthesized by sol−gel polymerization of titanium tetraisopropoxide using dialysis [6]. Silica cryogels have been synthesized with properties similar to those of silica aerogels, particularly in terms of particle morphology, density, porosity, and specific surface area [7]. These similarities can be explained by the high pressure produced by ice crystallites onto thin residual liquid films between these crystallites. The resulting conditions are similar to the high-pressure conditions used to synthesize aerogels. The textural characterization of silica cryogels was based on nitrogen adsorption isotherms, scanning electron microscopy (SEM) images, structural analysis using infrared (FTIR) and nuclear magnetic resonance (^{29}Si MAS NMR) spectra [7]. Titania–silica hydrogels were molded into various shapes, microhoneycomb, self-standing bundle, microfibers,

and powder, by a unidirectional freezing method [8]. Zeolite was synthesized by ice-templating and steam-assisted crystallization using a structure-directing agent, and silica gel as a precursor was prepared by applying ice-templating to the hydrogels synthesized from colloidal silica [9]. Hybrid SBA-15/carbon cryogel composites have been prepared by sol–gel polycondensation of resorcinol and formaldehyde followed by freeze drying, and subsequent pyrolysis [10]. Characterization of this material was accomplished using nitrogen adsorption, X-ray diffraction (XRD) and SEM methods. A highly conductive carbon cryogel, based on graphene and prepared by the sol–gel polymerization of resorcinol and formaldehyde in an aqueous surfactant, was characterized using nitrogen adsorption, XRD, FTIR, Raman spectroscopy, and SEM [11]. Carbon cryogels have been obtained by freeze-drying and pyrolysis of a family of tannin-formaldehyde organic gels prepared at different pH values [12]. The textural characteristics were analyzed by using nitrogen adsorption isotherms. It is worth mentioning that characterization of structurally more stable (rigid) solid inorganic cryogels is much easier than that of the softer and less rigid hydrated organic cryogels [5].

Inorganic cryogels are often synthesized by freezing sol-gel synthesis products in an aqueous solution, or a mixed organic/aqueous solution, followed by sublimation using a freeze-dryer. Cryogel synthesis can be considered an alternative means to synthesize materials similar to aerogels, as both synthetic methods involve high pressures. As yet there have been no reports dealing with the solid cryogel synthesis utilizing external pressures in special reactors working at very high pressures up to 1000 atmospheres.

The aim of this work was to synthesize silica cryogels (“cryosilicas”) at high external pressures using fumed silica A-300 as a precursor. This fumed material is formed by flame pyrolysis of $SiCl_4$. The resulting silica consists of solid nonporous primary nanoparticles of 8.3 nm in mean diameter and S_{BET} = 330 m^2/g. Cryogel powders synthesized at high pressures from this fumed silica were characterized utilizing high-resolution transmission electron microscopy (HRTEM), thermogravimetric analysis (TGA), adsorption of N_2 or Ar to determine the textural

characteristics, FTIR to probe surface hydroxyl groups, low-temperature ^{1}H NMR spectroscopy and thermally stimulated depolarization current (TSDC) to analyze the interfacial phenomena.

2. Materials and methods

2.1 Materials

Fumed silica A-300 (pilot plant of the Chuiko Institute of Surface Chemistry, Kalush, Ukraine; S_{BET} = 330 m^2/g) was used as the starting material. Aqueous suspensions of A-300 (5, 10, 15 and 20 wt.%) were prepared using doubly distilled water and sonicated (22 kHz) for 5 min. The resulting dispersion was then frozen at −14 ^{o}C in thick walled stainless steel reactors at pressures of 450 or 1000 atm, caused by ice formed in the frozen suspension (~10-15 ml) for 24 h. The pressure was estimated according to the literature [13-15], and was controlled using partial (450 atm) or complete (~1000 atm) filling of a freezing bomb with stainless steel. Then cryosilica (CS) samples were placed in a glass dish and dried in air at room temperature for 2-5 days to an air-dry state. The final materials were in the powder state.

2.2. ^{1}H NMR spectroscopy

^{1}H NMR spectra of static samples were recorded using a Varian 400 Mercury spectrometer (magnetic field 9.4 T) utilizing 90^o pulses of 3 μs duration. Each spectrum was recorded by coaddition of eight scans with a 2 s delay between each scan. Relative mean errors were less than ±10% for ^{1}H NMR signal intensity for overlapped signals, and ±5% for single signals. Temperature control was accurate and precise to within ±1 K. The accuracy of integral intensities was improved by compensating for phase distortion and zero line nonlinearity with the same intensity scale at different temperatures. Repeated measurements of samples gave identical spectra, within experimental error, at the same temperature. To prevent supercooling, spectra were recorded at T = 200 K (for samples precooled to this temperature for 10 min), then heated to 290 K at a rate of 5 K/min with steps ΔT = 10 K or 5 K (with a heating rate of 5 K/min for 2

min), and maintained at a fixed temperature for 8 min [16,17] for data acquisition at each temperature.

Cryosilicas CS20 ($C_{A\text{-}300}$ = 20 wt.% in the aqueous suspension frozen where ice produced a pressure of 450 atm) and CS20m (prepared at ~1000 atm) were studied at different degrees of hydration (h = 0.08, 0.75, 1.1 and 5.67 g of water per gram of dry silica). Hydration levels were controlled by addition of a known amount of water to a powder sample placed into an ampoule. Samples were equilibrated at 293 K for 1 h before NMR measurements. Experiments with methane were at a slightly increased pressure because an ampoule was linked to a rubber vessel with methane at 1.1 atm. Liquids (*n*-decane, chloroform, dimethylsulfoxide (DMSO), acetonitrile, water, or concentrated aqueous solutions of H_2O_2, HCl or CF_3COOH) were added to fill the total volume of a NMR ampoule with hydrated silica (the weight of dry silica was ~100 mg). After addition of hydrophobic decane, the sample was heated to 320 K for 1-2 min to remove air bubbles and to completely fill free pores of hydrated silica powder.

^{1}H NMR signals of static samples were observed only for mobile molecules due to the use of a relatively narrow 20 kHz bandwidth, the short transverse relaxation time of solids (*e.g.* OH groups at a silica surface), as well as frozen adsorbates. The latter include ice ($T_f \approx 273$ K), solid *n*-decane ($T_f \approx 243.3$ K), $CDCl_3$ ($T_f \approx 209$ K) and other co-adsorbates. This technique has been applied to a variety of adsorbates and solid and polymeric adsorbents, biomaterials, cryogels, *etc*.; and methods have been described in detail elsewhere [5,16,17].

To determine the chemical shift of the proton resonance (δ_H), tetramethylsilane (TMS) was used as an internal standard at δ_H = 0 ppm (or methane at δ_H = 0 ppm). The average errors in determination of the δ_H values in the temperature range studied were less than ±0.25 ppm.

The amount of unfrozen water (C_{uw}) as a function of temperature at T < 273 K was measured by comparing the total ^{1}H NMR integrated signal intensity of unfrozen water, I_{uw}, with that of all water at T > 273 K. This was done using a calibrated function $I_C = f(C_{H2O})$, assuming $C_{uw} = C_{H2O}\, I_{uw}/f(C_{H2O})$. The function $f(C_{H2O})$ was determined by measurements of the total

integral intensity of the ^{1}H NMR spectra after known amounts of water were added to the materials at T > 273 K. The low-temperature ^{1}H NMR spectroscopy provides structural information on interfacial water, pore structure (with cryoporometry and relaxometry), and thermodynamic characteristics of bound water or other liquids [16,17]. These characteristics include changes in Gibbs free energy caused by the adsorption (ΔG) of strongly bound water (SBW), $\Delta G_s < -0.5$ kJ/mol, and weakly bound water (WBW), $\Delta G_w > -0.5$ kJ/mol. In addition the amounts of SBW (C_{uw}^s) and WBW (C_{uw}^w) can be obtained. WBW is frozen at T > 255-260 K, while SBW is frozen at T < 255-260 K [16,17]. Furthermore, bound water can be assigned to strongly (SAW) or weakly (WAW) associated water based on chemical shift. A δ_H = 4-5 ppm indicates SAW with large 3D clusters or domains, chemical shifts of 1-2 ppm are indicative of WAW which consist of small 2D or strongly branched clusters.

According to the approximation of a Gibbs layer of finite thickness, surface forces act on a distance of several molecular layers. Changes in the Gibbs free energy of ice with temperature [18] have been calculated as follows:

$$\Delta G_{ice} = 0.0295 - 0.0413\Delta T + 6.64369\times10^{-5}(\Delta T)^2 + 2.27708\times10^{-8}(\Delta T)^3 \text{ (kJ/mol)}, \quad (1)$$

where $\Delta T = 273.16 - T$ at $T \le 273.15$ K. Equation (1) was used to estimate the $\Delta G(T)$ function for bound water [16]. The area under the $\Delta G(C_{uw})$ curve (the temperature dependence of $\Delta G(T)$ and amounts of unfrozen pore water $C_{uw}(T)$ can be transformed into the relationship $\Delta G(C_{uw})$) which determines overall changes in the Gibbs free energy of interfacial water as shown in Eq.(2),

$$\gamma_S = A\int_0^{C_{uw}^{max}} \Delta G dC_{uw}, \quad (2)$$

where C_{uw}^{max} is the total amount of unfrozen water at T = 273 K, and A is a unit dependent constant [16].

The freezing point depression for water in narrow pores is described by the Gibbs-Thomson relation (assuming a cylindrical pore shape) at radius R [17,19-22] given as Eq. (3);

$$\Delta T_m = T_{m,\infty} - T_m(R) = -\frac{2\sigma_{sl}T_{m,\infty}}{\Delta H_f \rho R} = \frac{k}{R}, \quad (3)$$

where $T_m(R)$ is the melting temperature of ice in cylindrical pores of radius R, $T_{m,\infty}$ the bulk melting temperature, ΔH_f the bulk enthalpy of fusion, ρ the density of the solid, σ_{sl} the energy of solid-liquid interaction, and k is a constant (here k = 67 K nm). Eq. (3) was used to determine the distribution function ($f_V(R) = dV_{uw}(R)/dR$) of sizes of water structures unfrozen at T < 273 K [17] and adsorbed onto nanosilicas. The $f_V(R)$ function can be used to determine the distribution function with respect to the specific surface area ($f_S(R)$) of water structures, and the size distribution of pores (PSD) filled by this water [17]. Integration of the $f_S(R)$ function gives the specific surface (S_{uw}) of contact area between unfrozen water and a solid surface [17]. Such contributions can be differentiated as nanopores at $R \le 1$ nm (S_{nano}), mesopores at $1 < R \le 25$ nm (S_{meso}), and macropores at $R > 25$ nm (S_{macro}). Frequently S_{uw} is less than S_{BET} due to partial filling of pores. Similar contributions to the pore volume can be calculated by integration of the $f_V(R)$ functions. The average melting temperature $<T_m>$ was calculated using Eq. (4) [17]

$$< T_m >= \int_{T_{min}}^{T_0} TC_{uw}(T)dT \Big/ \int_{T_{min}}^{T_0} C_{uw}(T)dT, \quad (4)$$

where T_0 = 273.15 K, and T_{min} is the temperature corresponding to C_{uw} = 0.

2.3. Fourier Transform Infrared Spectroscopy (FTIR)

The FTIR spectra of powdered samples over the 4000–300 cm^{-1} range (at 4 cm^{-1} resolution) were recorded in diffuse reflectance mode using a ThermoNicolet FTIR spectrometer, or in transmittance mode using a Specord M80 (Carl Zeiss, Jena) spectrometer using sample powder (~2 mg for all samples) located on a polished KBr glass plate (sample excess was shaken off), or in a stirred and pressed mixture with KBr (1 : 20 or 1 : 100, tables of ~20 mg for all samples). These spectra were re-calculated into the absorbance spectra.

2.4. Textural characteristics

The specific surface area (S_{Ar}) was calculated using adsorption of argon (from an Ar/He mixture) at 77.4 K with a LKhM-72 (Russia) chromatograph with Silochrome-80 as the reference material.

To analyze the textural characteristics of silicas, low-temperature (77.4 K) nitrogen adsorption–desorption isotherms were recorded using a Micromeritics ASAP 2405N adsorption analyzer. The specific surface area (S_{BET}) was calculated according to the standard BET method [23,24]. The total pore volume V_p was evaluated from the nitrogen adsorption at $p/p_0 \approx 0.99$ (p and p_0 denote the equilibrium and saturation pressure of nitrogen at 77.4 K, respectively). The nitrogen desorption data were used to compute the pore size distributions (PSDs, differential $f_V(R) \sim dV_p/dR$ and $f_S(R) \sim dS/dR$) using a self-consistent regularization procedure under non-negativity condition ($f_V(R) \geq 0$ at any pore radius R) at a fixed regularization parameter $\alpha = 0.01$ with a complex pore model with slit-shaped and cylindrical pores, and voids between spherical nonporous nanoparticles packed in random aggregates (SCV/SCR model) [25,26]. The differential PSDs (SCV/SCR with respect to pore volume $f_V(R) \sim dV/dR$, $\int f_V(R)dR \sim V_p$) were re-calculated to incremental PSD (IPSD, $\Phi_V(R_i) = (f_V(R_{i+1}) + f_V(R_i))(R_{i+1} - R_i)/2$ at $\sum\Phi_V(R_i) = V_p$). The differential $f_S(R)$ functions were used to estimate the deviation (Δw) of the pore shape from the model [27]. The $f_V(R)$ and $f_S(R)$ functions were also used to calculate contributions of nanopores (V_{nano} and S_{nano} at $0.35 < R < 1$ nm), mesopores (V_{meso} and S_{meso} at $1 < R < 25$ nm), and macropores (V_{macro} and S_{macro} at $25 < R < 100$ nm) to the total pore volume and the specific surface area.

2.5. Thermogravimetry (TG)

Desorption of water from silicas was investigated over the 293–1273 K range by means of TG in air using a Derivatograph C (Paulik, Paulik, & Erdey, MOM, Budapest) at a heating rate of 10 K/min. The TG data was used to compute the pore size distribution (PSD) using a thermoporometry method described in detail elsewhere [28].

2.6. Thermally stimulated depolarization current (TSDC)

The tablets (diameter 30 mm, thickness ~1-3.5 mm) with the frozen aqueous suspension of fumed silica A-300 (C_{SiO2} = 5 wt% (cryosilica CS5 prepared at 1000 atm, CS5m) or 20 wt% (gel at standard conditions)) or dried CS5m (hydration h = 1.6 g/g) and CS20m (h = 1.6 g/g) were polarized by the electrostatic field at the intensity $F \sim 3\times10^5$ V/m at 263 K (suspensions) or 271 K (powders) then cooled to 80-90 K with the field still applied and heated without the field at a heating rate β = 4 K/min. The current evolving due to sample depolarization [29] was recorded by an electrometer over the 10^{-15}-10^{-5} A range. Relative mean errors for TSDC measured were δ_I = ±5%, δ_T = ±2 K for temperature, δ_β = ±5% for the temperature change rate. To compare TSDC thermograms of different systems, they were normalized to $F = 1\times10^5$ V/m with consideration of the tablet thickness.

2.7 HRTEM

High resolution transmission electron microscopy, HRTEM (JEM-2100F, Japan) images were recorded for initial A-300 and cryosilica CS20m. A powder sample was added to acetone (for chromatography) and sonicated. Then a drop of the suspension was deposited onto a copper grid with a thin carbon or polymeric film. After acetone evaporation, sample particles remained on the film were studied with HRTEM.

3. Results and discussion

3.1. Effects of freezing conditions on the particle morphology and aggregate texture

The freezing of aqueous suspensions of nanosilica in high-pressure reactors results in dried powdered materials that are very different from silicas treated in vapor phase water at high pressures and temperatures [30-37], at high temperatures and normal pressure in air [38], or at room temperature and normal pressure followed by air drying [39-41]. The air-dried high-

pressure cryosilicas are in the powder state with agglomerates of 1-20 μm in size (Fig. 1), which is far more compacted than in the fumed silica starting material.

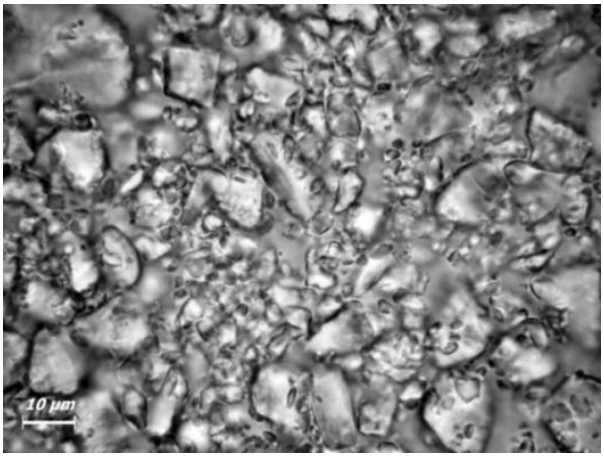

Fig. 1. Microphotograph (Primo Star optical microscope, Carl Zeiss) of CS20m powder prepared at 1000 atm (scale bar 10 μm).

The bulk density of the cryosilica powder, as well as of any suspended and dried nanosilicas, increases approximately five-fold (Table 1, ρ_b), since ρ_b = 0.045 g/cm^3 for the initial A-300 powder. This is due to re-arrangement of nanoparticles in aggregates and agglomerates of aggregates during suspension and subsequent drying. Primary particles become mobile in sonicated aqueous suspensions including a large proportion of individual nanoparticles [32-41]. During drying of the suspensions, nanoparticles tend to form more compacted aggregates and agglomerates than those formed in the flame (flow velocity > 20 m/s) during pyrogenic synthesis [32-41]. There is empty volume ($V_{em} = 1/\rho_b - 1/\rho_0$) of the powder, which is directly links to the bulk density ρ_b and true density (ρ_0 = 2.2 g/cm^3) of silicas. Typically, the pore volume (Table 1, V_p) determined from the adsorption of nitrogen at p/p_0 = 0.98-0.99 is much smaller than V_{em}. For example, for initial fumed silica (ρ_b = 0.045 g/cm^3) V_{em} = 21.8 cm^3/g, but V_p = 0.65 cm^3/g is much smaller because nitrogen cannot effectively fill large pores, especially at R > 100 nm. For suspended-frozen-dried silica CS20m ρ_b = 0.31 g/cm^3 and V_{em} = 2.8 cm^3/g but V_p = 1.28 cm^3/g; i.e. the difference between the V_{em} and V_p values strongly decreases after cryogelation. These

textural changes are readily observed in the HRTEM images (Figs. 2 and 3), IPSD (Fig. 4a-e) and nitrogen adsorption isotherms (Fig. 4f).

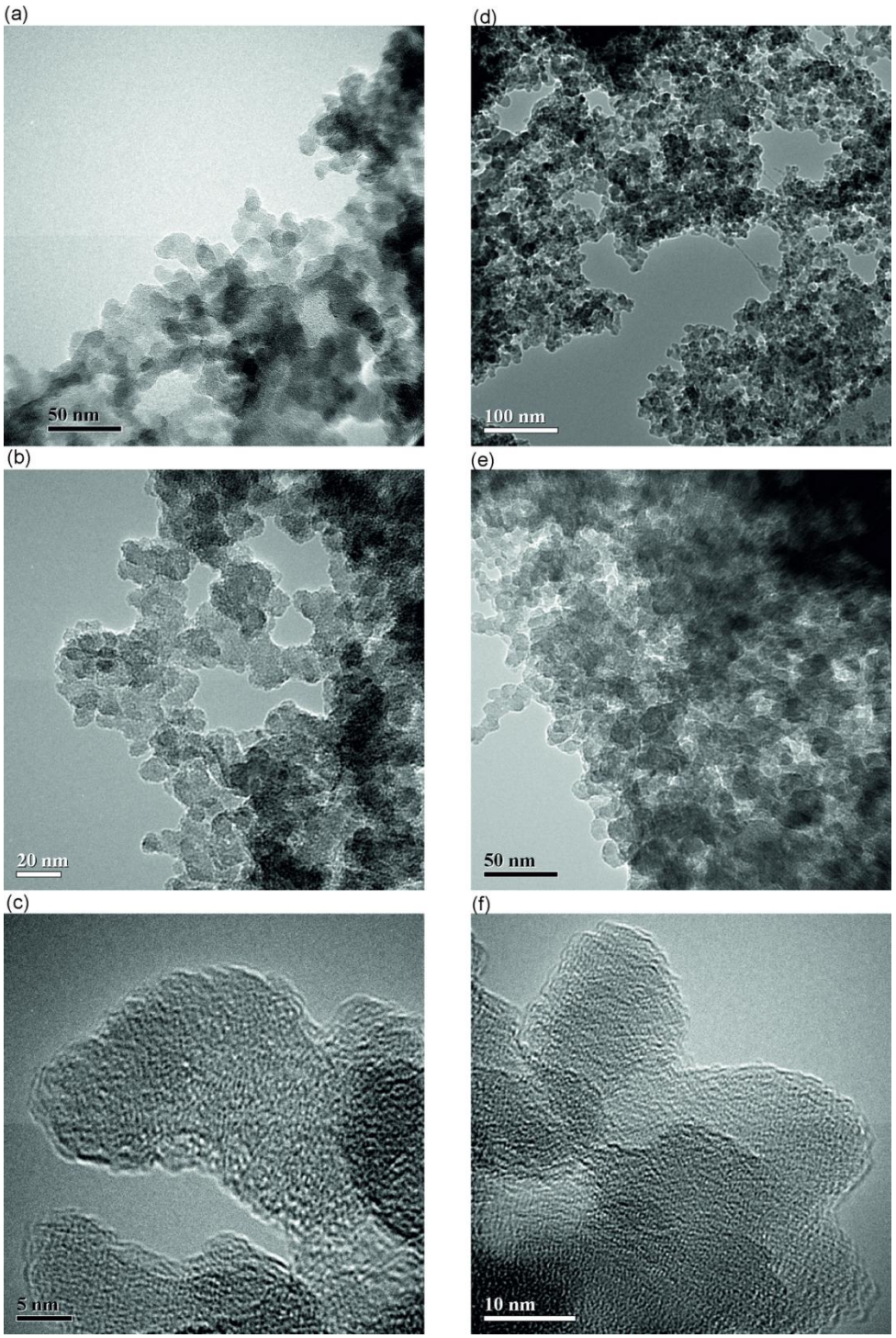

Fig. 2. HRTEM images of (a, b, c) initial A-300 and (d, e, f) CS20m at different magnifications (scale bars (d) 100 nm, (a, e) 50 nm, (b) 20 nm, (f) 10 nm, and (c) 5 nm).

According to HRTEM images (Fig. 2), CS20m is composed of amorphous primary particles more strongly compacted in aggregates (comp. Fig. 2a,e). These aggregates remained

porous with the textural porosity as voids between nonporous primary particles (Fig. 2d). The shape of primary particles is not ideally spherical for both initial A-300 and CS20m.

Table 1
Textural (specific surface area S_{Ar} and S_{BET}), bulk density (ρ_b) and adsorption (desorption of water in TG) characteristics of silicas *vs*. silica content in the frozen suspension ($C_{A\text{-}300}$), pressure and treatment temperature (T_{tr}).

Sample	$C_{A\text{-}300}$ (wt.%)	S_{Ar}[a] (m^2/g)	S_{BET} (m^2/g)	V_p (cm^3/g)	S_{nano} (m^2/g)	S_{meso} (m^2/g)	S_{macro} (m^2/g)	V_{nano} (cm^3/g)	V_{meso} (cm^3/g)	V_{macro} (cm^3/g)	Δw
Initial			330	0.826	51	270	9	0.026	0.653	0.147	0.025
CS5	5	317	280	1.474	14	258	8	0.009	1.358	0.107	0.392
CS10	10	303	293	1.341	23	268	1	0.015	1.294	0.032	0.431
CS15	15	295	292	1.347	29	262	1	0.019	1.289	0.039	0.454
CS20	20		297	1.279	33	263	1	0.022	1.231	0.026	0.463
CS20m	20		285	1.277	31	253	1	0.021	1.220	0.037	0.458
CS5*	5	332	286	1.393	10	275	1	0.006	1.364	0.023	0.363
CS10*	10	326	289	1.298	15	272	2	0.010	1.247	0.041	0.459
CS15*	15	323	304	1.470	27	276	1	0.017	1.423	0.029	0.401
CS20*	20	306	303	1.443	20	281	2	0.013	1.402	0.028	0.404
CS5**	5	302	300	1.449	24	273	2	0.015	1.390	0.044	0.389
CS10**	10	318	303	1.445	23	278	2	0.014	1.390	0.041	0.405
CS15**	15		304	1.455	19	281	3	0.012	1.390	0.053	0.397
CS20**	20	317	296	1.408	36	257	3	0.023	1.328	0.056	0.451

Sample	ρ_b (g/cm^3)	Intact water[b] (T < 200°C) (mmol/g)	Total water[c] (T < 900°C) (mmol/g)	ΔW[d] (W_{200}–W_{600}) (mmol/g)	c_{void}	c_{cyl}	c_{slit}	Pressure (atm)	T_{tr} (°C)
Initial	0.045	0.889	1.556	0.383	0.308	0.368	0.324	-	-
CS5	0.235	0.619	3.417	1.780	0.159	0.611	0.230	450	-14
CS10	0.208	1.238	2.600	0.744	0.197	0.387	0.416	450	-14
CS15	0.228	0.745	1.397	0.537	0.194	0.268	0.538	450	-14
CS20	0.294	5.177	6.225	0.798	0.203	0.203	0.622	450	-14
CS20m	0.309	1.556	3.103	0.962	0.209	0.171	0.620	1000	-14
CS5*	0.285	12.742	13.545	0.708	0.182	0.695	0.123	1	-14
CS10*	0.294	2.596	4.035	1.005	0.227	0.380	0.393	1	-14
CS15*	0.349	1.977	2.924	0.731	0.163	0.458	0.379	1	-14
CS20*	0.282	2.290	3.047	0.609	0.151	0.555	0.294	1	-14
S5**	0.277	1.711	3.202	1.170	0.180	0.522	0.298	1	25
S10**	0.311	1.630	3.204	1.143	0.174	0.522	0.304	1	25
S15**	0.216	2.054	3.692	1.011	0.168	0.565	0.268	1	25
S20**	0.202	1.576	5.894	1.548	0.185	0.223	0.592	1	25

Notes. [a]Samples were heated at 100 °C for 2 h before measurements of the specific surface area. The amounts of water desorbed during heating from [b]20 °C to 200 °C, [c]20 °C to 900 °C, and [d]200 °C to 600 °C.

The interatomic distances calculated from HRTEM images of nanoparticles (Fig. 2c,f) using Fiji software with local thickness plugin [42] are similar for initial A-300 and CS20m (Fig. 3). However, the average value $< d >= \int df(d)\mathrm{d}d / \int f(d)\mathrm{d}d$ (*i.e*. the first moment of the distribution function) is smaller for CS20m (<*d*> = 0.3766 nm) than for initial A-300 (<*d*> = 0.3979 nm). Thus, high-pressure cryogelation results in not only stronger aggregation of primary particles (the bulk density ρ_b (Table 1) increases) but also in certain deformation of nanoparticles (the <*d*>

value decreases). Changes in the textural porosity of treated nanosilica reflected in changes in the ρ_b value can be analyzed using the pore size distributions (Fig. 4).

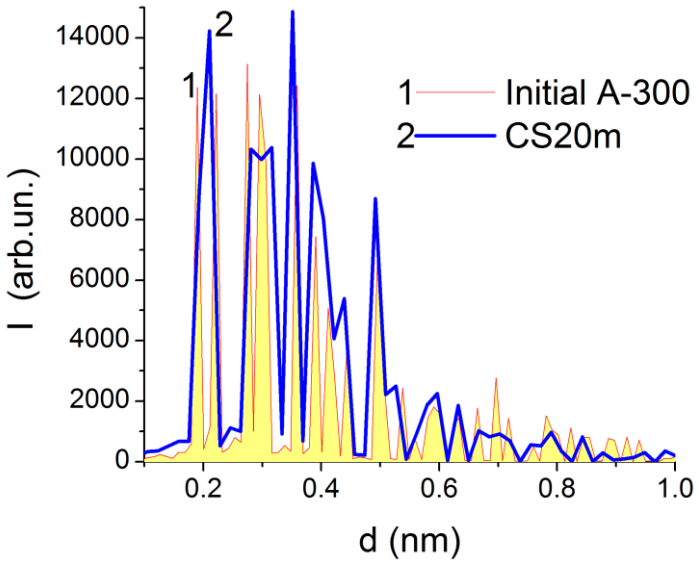

Fig. 3. Interatomic distances in primary particles of (1) initial silica A-300 and (2) cryosilica CS20m calculated using HRTEM images (Fig. 2c,f) treated with Fiji software (local thickness plugin).

For treated silica powders, contribution of nanopores and narrow mesopores decreases, while the contribution of mesopores at R = 10-30 nm increases compared with the initial fumed silica A-300 (Fig. 4, Table 1). The primary particles are not strongly changes during suspending-cryogelation-drying (Figs. 1 and 2). Therefore, the nitrogen adsorption isotherms are practically the same at $p/p_0 < 0.8$ (Fig. 4f, insert) but they characterized by different hysteresis loops at $p/p_0 > 0.8$ and different maximal adsorption at $p/p_0 \approx 0.99$ (Fig. 4f). These results show significant changes in packing of primary particles in aggregates. This packing increases with increasing pressure during cryogelation. Additionally, the effect becomes stronger with increasing silica content in the suspensions (comp. Fig. 4a-e).

An increase in the silica content in the suspensions results in an increase in mesopore contribution at $R \approx 10$ nm, and in a decreased contribution of mesopores at $R \approx 20$ nm for high-pressure cryosilicas in contrast to samples prepared at standard pressure. The main PSD peak (both IPSD and dV/dR, Fig. 4) for HP-cryosilicas shifts toward smaller R values with increasing silica content in the suspensions.

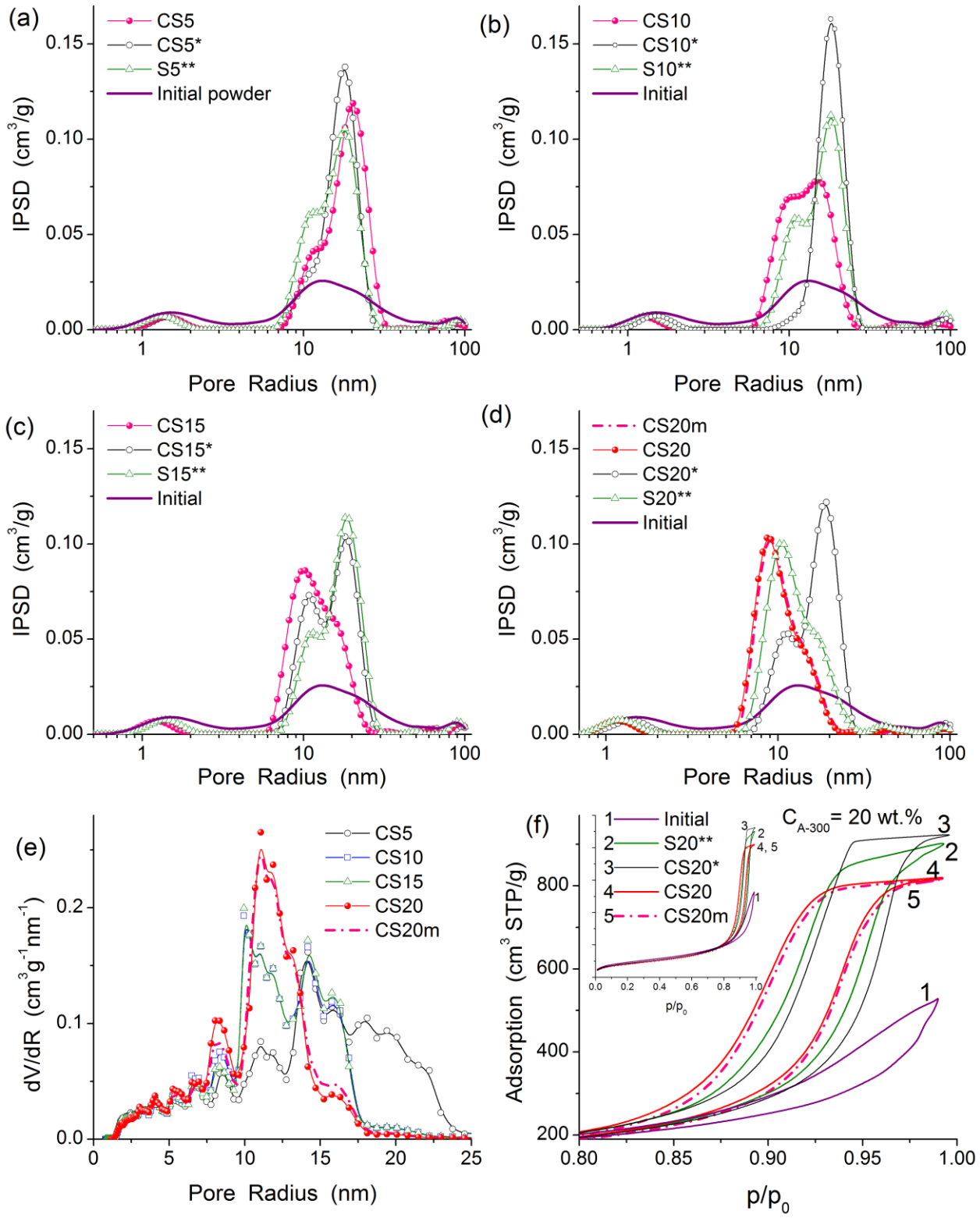

Fig. 4. Incremental PSD (SCV/SCR) for initial powder of A-300 and silicas prepared at $C_{A\text{-}300}$ = (a) 5 wt.%, (b) 10 wt.%, (c) 15 wt.% and (d) 20 wt.% in the aqueous suspensions under different conditions: frozen at high pressure (450 atm) or at maximum high pressure (1000 atm), frozen at normal pressure (*), suspended under normal conditions (**), as well as initial A-300 powder, (e) NLDFT for cryosilicas prepared from 5-20 wt.% suspensions and CS20m; (f) nitrogen adsorption-desorption isotherms for differently treated samples at $C_{A\text{-}300}$ = 20 wt.%.

Additionally HP-cryosilicas, in contrast to silicas frozen or non-frozen at normal pressure, the contribution of pores modeled by slit-shaped pores (Table 1, c_{slit}) increases due to the high-pressure effects. This effect is due to certain changes in the shape of primary particles (Figs. 2 and 3), which are discussed above.

Contributions of nanopores (Fig. 4, Table 1, S_{nano} and V_{nano}) and macropores (S_{macro} and V_{macro}) are much smaller than that of mesopores (S_{meso} and V_{meso}) for all silicas treated in the aqueous media under different conditions. However, in contrast to V_{meso}, the S_{nano}, S_{macro}, V_{nano}, and V_{macro} values for treated silicas decrease in comparison with the initial silica. The S_{meso} values for high-pressure cryosilicas are smaller than that for the initial silica but the S_{meso} values for normal-pressure cryosilicas (Table 1, label *) and non-frozen suspended-dried silicas (label **) are larger than that of the initial silica. All these textural changes are due to different rearrangement of aggregates of primary nanoparticles depending on treatment conditions.

3.2. Surface properties of cryosilicas

The bands in the range of non- or slightly interacting O-H stretching vibrations of silanols (Fig. 5, 3750-3700 cm^{-1}) as well as overtone vibrations and combination bands (2000-1500 cm^{-1}) [33-36] are of low intensity in comparison with the initial nanosilica. This effect is more pronounced for the sample prepared from the most concentrated suspension, $C_{A\text{-}300}$ = 20 wt.% (CS20). Therefore, one can conclude that the FTIR spectra are consistent with changes in the bulk density, increase of which indicates increased particle aggregation. CS20 and CS15 adsorb certain amounts of water characterized by a band at 1600 cm^{-1} (deformation vibrations) a broad band at 3600-2700 cm^{-1} (OH-stretching vibrations) which also includes hydrogen bonded silanols. This water disturbs practically all the surface hydroxyls, and the band of free silanols is much weaker (Fig. 5b, curves 1 and 2) than that of the heated initial silica (Fig. 5b, curve 4). Notice that cryosilica powder after heating to 900 ^{o}C (during TG experiment) and cooled to room temperature in air (Fig. 5, curve 4) contains low amounts of both adsorbed water (compare with

curve 3 in the both ranges of 1600 and 3600-2700 cm^{-1}) and free silanols (compare with curve 5) due to their condensation during heating. In the case of initial nanosilicas containing 1-7 wt.% of adsorbed water the band of free silanols is readily observed [33-36,43], but in the case of porous silicas containing about 10 wt.% of adsorbed water, this band is not observed similar to the spectra for silica gels. This can be due to enhanced aggregation of nanoparticles in high-pressure cryosilicas. After cryogelation, the asymmetric band of the Si-O_{Si} stretching vibrations (Fig. 4a) is narrower for CS20m than for CS20 or CS15. This suggests that CS20m is composed of more aggregated particles.

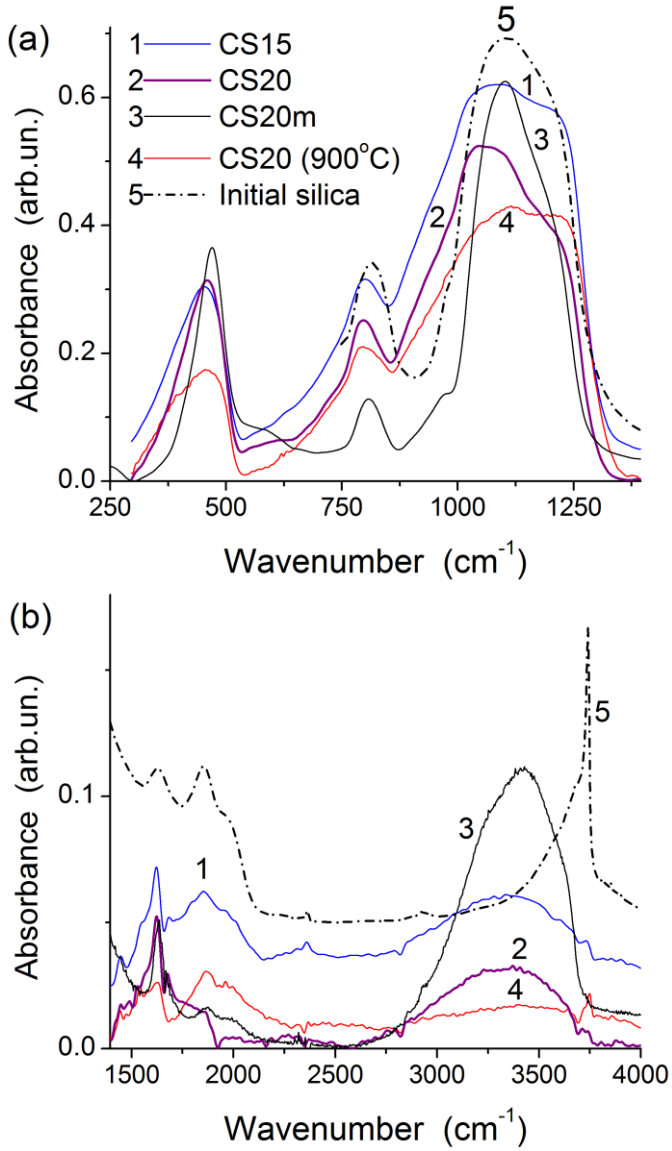

Fig. 5. FTIR spectra of high-pressure silica cryogels prepared using suspensions at $C_{A\text{-}300}$ = 15 wt.% (CS15, curve 1) and 20 wt.% CS20 (curve 2) and CS20m (curve 3), and CS20 heated at 900 °C – curve 4) and dehydrated initial nanosilica (curve 5) in (a) low and (b) high wavenumber ranges.

Another method to probe water content in the powder materials is thermogravimetric (TG) and differential thermogravimetric (DTG) analyses (Fig. 6).

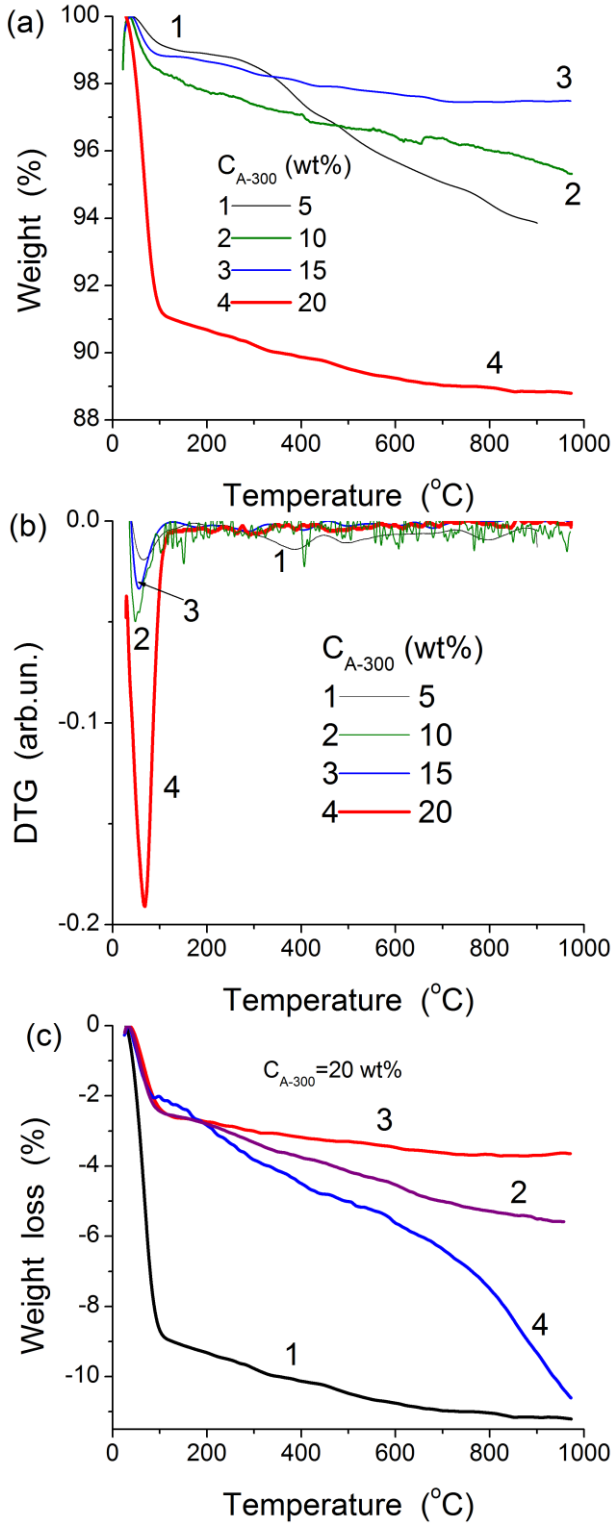

Fig. 6. Thermogravimetric (a, c) (TG) and (b) differential TG (DTG) data for air-dry high-pressure cryosilicas prepared at 450 atm and different concentrations $C_{A\text{-}300}$ (a, b), (c) cryogels CS20 (curve 1), CS20m (2), and CS20* (3) and unfrozen gel dried S20** (4).

The most concentrated sample, $C_{A\text{-}300}$ = 20 wt.% (CS20) prepared at 450 atm, contains the greatest amount of adsorbed intact water (~9 wt.%, desorbed at T < 200 ^{o}C) of the prepared samples (Fig. 6a). However, more complex TG and DTG curves are observed for CS5 (Fig. 6a). A similar TG curve (but with a greater amount of desorbed water) is observed for dried gel prepared at normal pressure without freezing (Fig. 6c, curve 3). Notice that cryogel $C_{A\text{-}300}$ = 20 wt.% prepared at normal pressure contains a much smaller amount of adsorbed water similar to high-pressure cryogels but prepared using less concentrated suspensions (Fig. 6a).

In the case of high-pressure cryogels, there are two tendencies: (i) a certain decrease in the specific surface area (Table 1, S_{Ar} and S_{BET}) with increasing silica content in the suspension, and (ii) nonlinear changes in the amounts of desorbed water (total water desorbed at T < 900 ^{o}C) with a maximum for the material prepared at $C_{A\text{-}300}$ = 5 wt.% (Table 1). Both tendencies remain for cryogels prepared at normal pressure (Table 1, CS-X*). Thus, the desorbed water amounts (intact and total water) change with increasing silica content in the suspension. This can be explained by the formation of more compacted secondary structures with increasing $C_{A\text{-}300}$ value, changes in the sizes of pores filled by water, and the number of hydroxyls. Notice that changes in the specific surface area depend on the preparation conditions (C, P, T) much less than the pore volume (V_p) and the content of desorbed water (Table 1). These results can be explained by greater changes in the organization of primary silica nanoparticles in secondary structures (Table 1, Fig. 4), with less change in nanoparticle size (Figs. 2 and 3), *e.g.*, observed during hydrothermal treatment of silicas [37].

3.3. Interfacial behavior of adsorbates bound to cryosilicas

Since CS20 and CS20m exhibit the largest structural changes among high-pressure cryosilicas, low-temperature ^{1}H NMR spectroscopy studies focused on these materials. In these studies water was either the sole probe compound or it was used as a co-adsorbate with different organics in various dispersion media (Figs. 7-12, Table 2) for deeper insight into the interfacial

behavior of different adsorbates and co-adsorbates such as nonpolar methane and *n*-decane, weakly polar chloroform, and polar water, DMSO, acetonitrile, H_2O_2, HCl, and CF_3COOH.

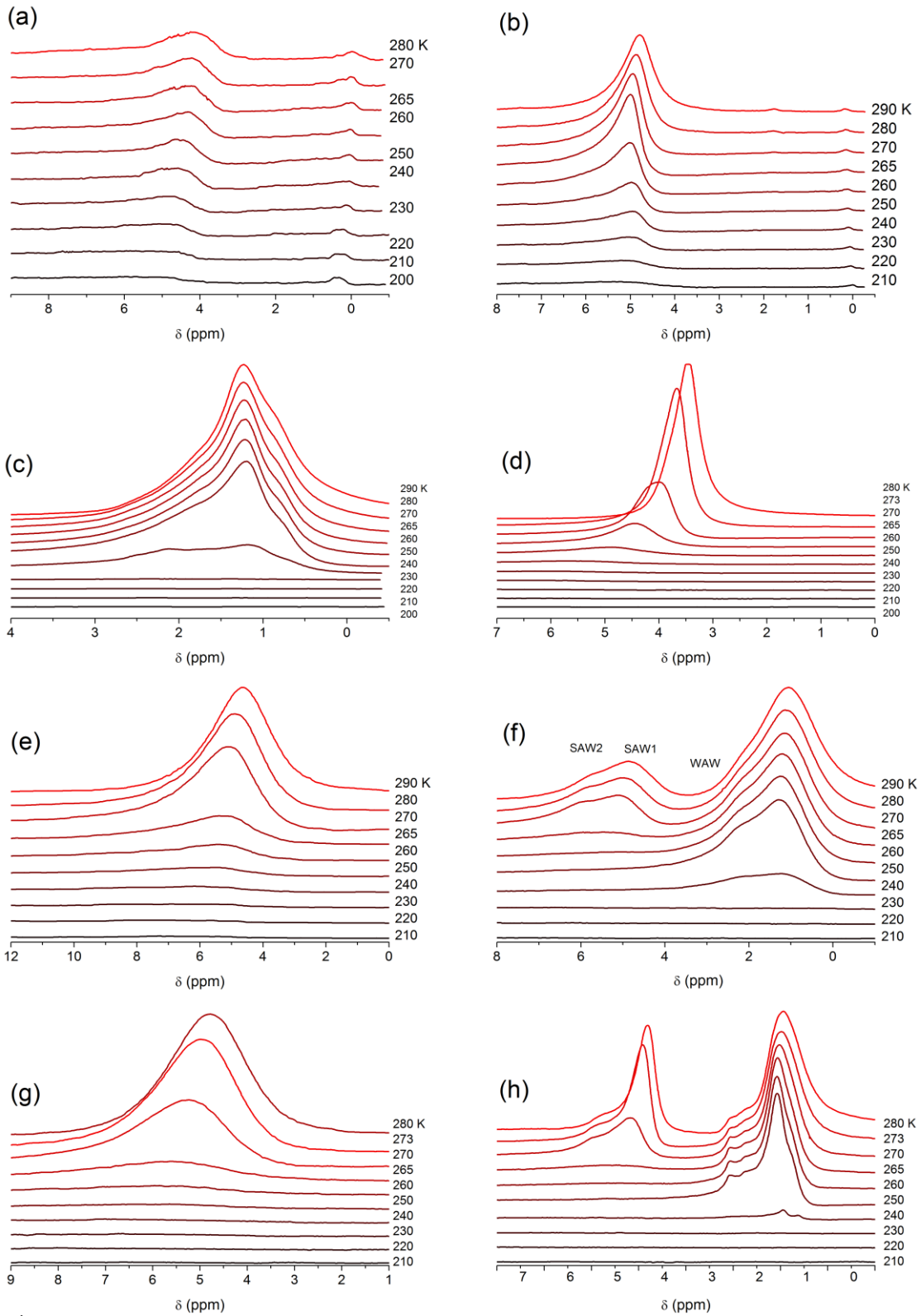

Fig. 7. ^{1}H NMR spectra of water bound to CS20 in different dispersion media at hydration degree *h* = (a-c) 0.08, (d) 5.67, (e, f) 0.75, (g, h) 1.1 g/g: (a) methane, (b) chloroform-*d*, (c, f, h) *n*-decane; (d) aqueous suspension; and (e, g) air.

CS20 (cryogelation at 450 atm) studied by NMR contained 0.08 g of water per gram of dry silica. To analyze the interfacial behavior of bound water, the sample was studied in different dispersion media as detailed in Figure 7. In the methane dispersion medium (Fig. 7a), the spectra of bound water include a single signal exhibiting a chemical shift (with respect to methane of δ_H = 0 ppm), $\delta_H \approx$ 4-5 ppm. This is similar to the δ_H value of bulk water. Consequently, this water can be assigned to strongly associated water (SAW), with an average number of hydrogen bonds per molecule of 3-4, similar to that in bulk water.

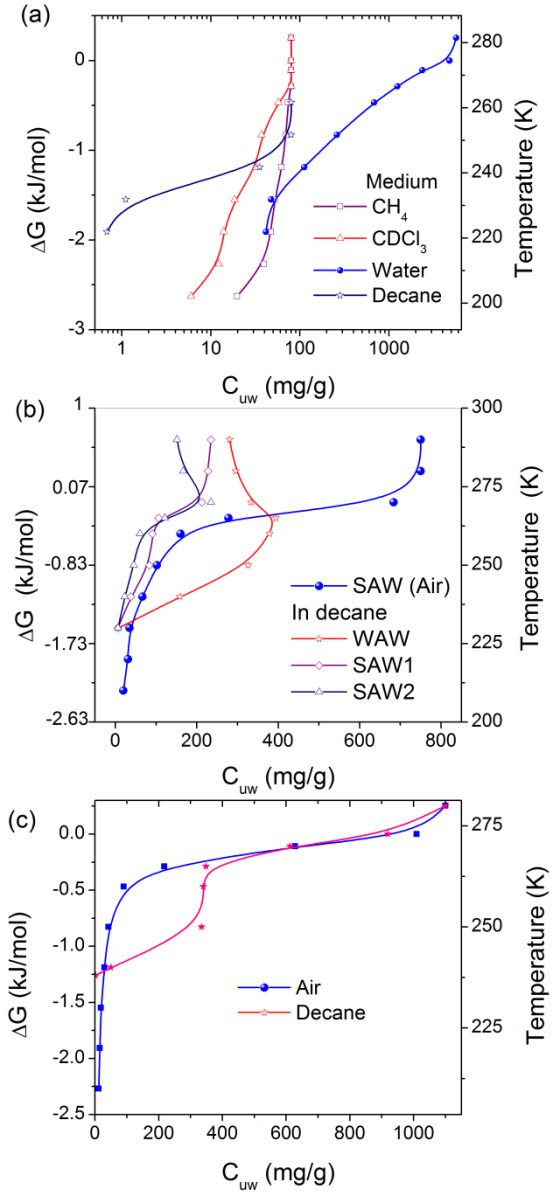

Fig. 8. Temperature dependences of the amounts of unfrozen water ($C_{uw}(T)$) and changes in the Gibbs free energy ($\Delta G(T)$) of bound water as well as relationships between C_{uw} and ΔG for CS20 in different dispersion media at (a) h = 0.08 g/g (in methane, chloroform, or decane) and 5.67 g/g (concentrated 15% suspension); (b) h = 0.75 g/g and (c) h = 1.1 g/g (in air or decane).

Freezing of bound water occurs at low temperatures at $T < 260$ K (Figs. 7a and 8) because of the freezing point depression for liquids confined in pores [16,17,19-22]. Since freezing of bound water occurs at $T < 260$ K, all of this water can be assigned to strongly bound water (SBW). The ^{1}H NMR signal of methane at $\delta_H \approx 0$ ppm (Fig. 7a) has a weak dependence on temperature. From the intensity ratio of water (h = 0.08 g/g) and methane, the amount of adsorbed methane can be estimated as small as ~8 mg/g at 280 K. This low adsorption of CH_4 is due to filling of nanopores (voids between adjacent nanoparticles, Figs. 2 and 4) by water (Fig. 9, Table 2), which methane cannot displace. This is because methane has much weaker interactions with the silica surface compared to water [17].

In the $CDCl_3$ dispersion medium, bound water (h = 0.08 g/g) corresponds to SAW characterized by $\delta_H \approx 5$ ppm (Fig. 7b). A fraction of this water becomes weakly bound (WBW) [16,17] frozen at $T > 260$ K. Additionally, at higher temperatures, a weak signal is observed at $\delta_H \approx 1.8$ ppm corresponding to weakly associated water (WAW) [16,17]. The signal at $\delta_H \approx 0$ ppm corresponds to tetramethylsilane used as a chemical shift standard. In contrast to methane, weakly polar chloroform diminishes the interaction of water with silica: the average melting temperature (Table 2, $<T_m>$), filling of mesopores by unfrozen water (V_{meso}, S_{meso}), and changes in the Gibbs free energy of the first layer (ΔG_s) of bound water increase; while the free surface energy (γ_S), filling of nanopores (V_{nano}, S_{nano}), and the SBW content decrease. Similar effects have been previously observed for different adsorbents due to the displacement of water by weakly polar chloroform from narrow to broader pores or out of pores altogether [17]. The main driving force of these effects leads to a reduction of the contact area between immiscible polar (water) and weakly polar (chloroform) or nonpolar (decane) liquids. This reduction results in a free energy decrease because water-water interactions are similar to water-silica interactions, but interactions of organic co-adsorbates with silica are stronger than that of organics-organics or organics-water interactions [16,17]. The character of re-organization of bound water under the action of

chloroform is seen in changes in the PSD, and in particular the IPSD, (Fig. 9b) when compared with water bound to CS20 in the methane dispersion medium (Fig. 9a).

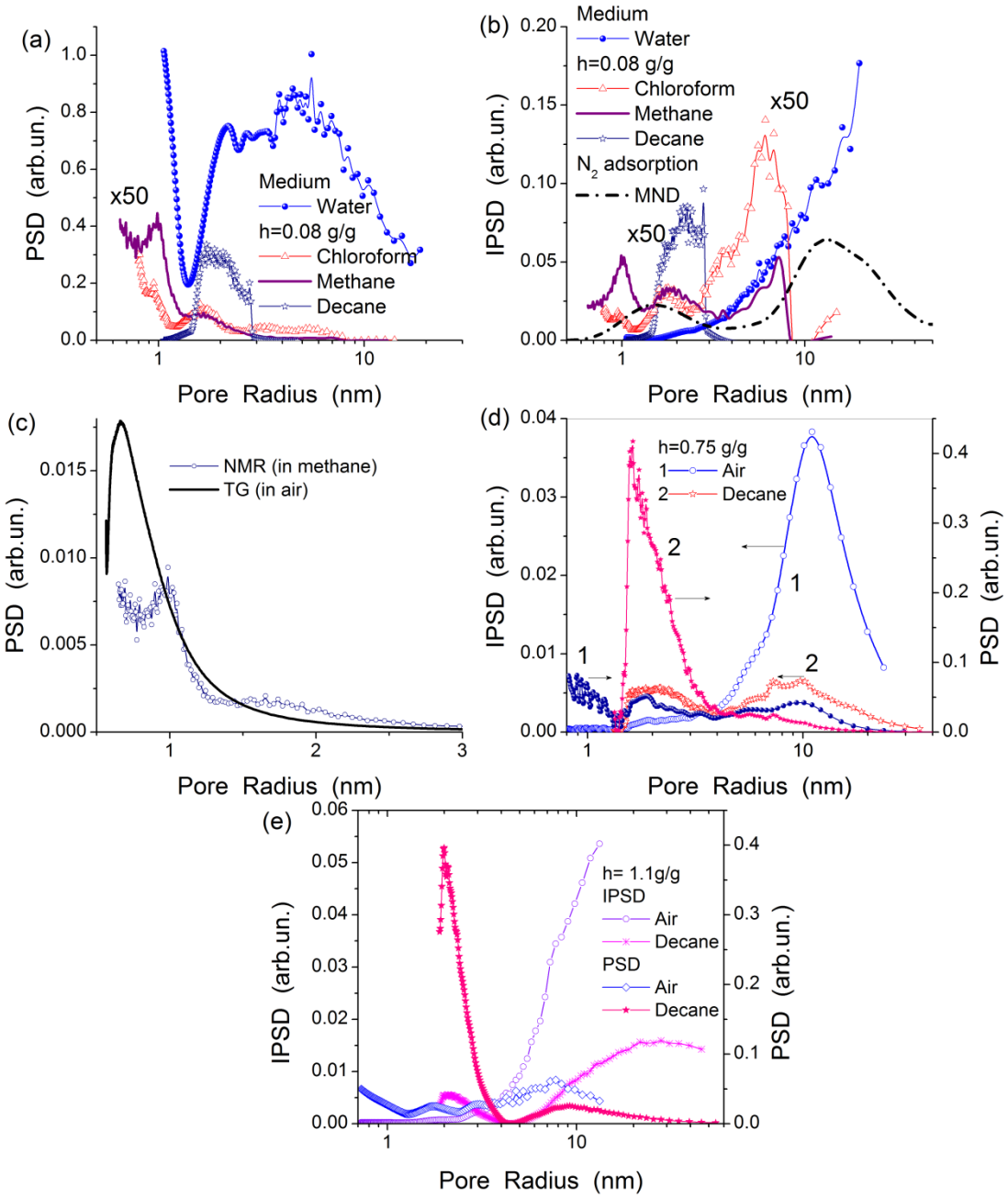

Fig. 9. Pore size distributions (a, c, d) differential and (b, d) incremental calculated using NMR cryoporometry (calculated as size distributions of water structures unfrozen in pores) (IPSD for initial A-300 was calculated using nitrogen adsorption-desorption isotherm, dot-dashed line), (c) NMR cryoporometry and TG thermoporometry curves; (d) h = 0.75 g/g and 1.1 g/g (air or decane dispersion media) for CS20 in different dispersion media; (a-d) CS20 and (e) CS20m samples.

Nonpolar *n*-decane more effectively displaces bound water than weakly polar chloroform (Figs. 7-9, Table 2). This result can be explained by much greater dispersion interactions of larger decane molecules with the silica surface than small methane or chloroform molecules. Notice that

similar effects of the water displacement are observed for small but polar molecules such as acetonitrile. Adsorbed decane demonstrates two ^{1}H NMR signals at 0.9 and 1.25 ppm (Fig. 7c) corresponding to methyl and methylene groups, respectively. The water signal is weak due to the relatively small amount compared to the decane content, and observed at $\delta_H \approx 1.8 – 2.5$ ppm (Fig. 7c). However, at h = 0.75 g/g, the water signal is much more intense but remains lower than the decane signal (Fig. 7f). The water observed is a WAW-SAW mixture, with a major contribution of SBW since it is frozen at T < 260 K. However, this water is more weakly bound to silica than that in either the methane or chloroform media (Fig. 8). The WBW content increases with increasing water content (Table 2, C_{uw}^{w}), this leads to an increase in the $<T_m>$ value. This is because the relative content of SBW decreases significantly from 75-100% (h = 0.08 g/g), 20-40% (h = 0.75 g/g) to 14% at (h = 5.67 g/g). Both highly hydrated powder CS20 at h = 0.75 g/g, and the concentrated (15%) aqueous suspension at h = 5.67 g/g, exhibit strongly and weakly bound water (Table 2).

Table 2
Characteristics of water bound to cryosilica powder CS20 and CS20m in different media.

h (g/g)	Medium	C_{uw}^{s} (g/g)	C_{uw}^{w} (g/g)	$-\Delta G_s$ (kJ/mol)	$-\Delta G_w$ (kJ/mol)	γ_S (J/g)
0.08	Methane	0.08	-	3.50	-	9.1
0.08	$CDCl_3$	0.06	0.02	2.97	0.47	5.2
0.08	Decane	0.08	-	2.23	-	5.7
0.75	Air	0.30	0.45	2.91	0.50	18.9
0.75	Decane	0.14	0.61	1.88	0.35	38.3
5.67	Water	0.80	3.27	2.34	0.30	67.4
0.1#[a]	Air	0.08	0.02	2.77	0.39	7.8
0.1#[b]	Air	0.08	0.02	2.78	0.44	8.0
1.1#	Air	0.21	0.890	3.21	0.35	15.0
1.1#	Decane	0.34	0.760	1.35	0.5	24.7
h (g/g)	$<T_m>$ (K)	S_{uw} (m^2/g)	S_{nano} (m^2/g)	S_{meso} (m^2/g)	V_{nano} (cm^3/g)	V_{meso} (cm^3/g)
0.08	216.2	89	71	18	0.03	0.05
0.08	241.8	45	21	24	0.01	0.07
0.08	240.0	65	0	65	0	0.08
0.75	259.7	115	32	83	0.01	0.67
0.75	248.5	110	0	110	0	0.74
5.67	260.9	301	0	301	0	4.10
0.1#[a]	229.6	41	36	5	0.02	0.07
0.1#[b]	229.0	42	36	6	0.02	0.07
1.1#	261.0	103	23	80	0.01	0.52
1.1#	258.4	84	0	78	0	0.67

Note. #CS20m, and other samples are based on CS20; CS20m stored at [a] 298 K and [b]255 K for a week.

Figure 7d exhibits a δ_H increase from 3.5 to 5.5 ppm (h = 5.67 g/g), or 4.5 to 5.5 ppm (h = 0.75 g/g) with decreasing temperature from 280 to 200 K. However, the amount of WBW is much larger than the amount of SBW, especially at h = 5.67 g/g (Table 2). This is a typical result for aqueous suspensions of nanosilicas [16,17]. Water adsorbed onto CS20 at h = 0.75 g/g can be divided into SBW and WBW, frozen at lower and higher temperatures, respectively. SAW (Fig. 7e, Table 2) is also found in the suspension. This effect can be explained by the formation of clusters and domains of water (Fig. 9d) which are not spatially separated. When this sample at h = 0.75 g/g is in the decane dispersion medium, the characteristics of bound water change quite a bit (Figs. 7f, 8b, and 9d, Table 2). WAW and two types of SAW appear, and the PSD becomes bimodal.

Notice that even at a low adsorbed water content (h = 0.08 g/g), there is a broad PSD (Fig. 9a,b) including clusters at $1 < R < 2$ nm and domains at $2 < R < 20$ nm. These structural features exhibit traces of the IPSD (determined from the nitrogen adsorption isotherm) characteristic of the initial fumed silica (Fig. 8b, dot-dashed line) which contained mesopores at $2 < R < 10$ nm. However, smaller and larger pores (voids between nonporous nanoparticles) differ because of the rearrangement of primary nanoparticles in the secondary structures due to suspension, cryogelation at high pressure (CS20 was prepared at 450 bar), and drying in air.

Results thus far have addressed systems using co-adsorbates that are either non- or much less polar than H_2O. It is of interest to study the systems with CS20 containing water co-adsorbed with more polar compounds such as H_2O_2, HCl, and CF_3COOH.

A 30% aqueous solution of H_2O_2 (0.05 g per gram of dry CS20) was added to CS20 preheated at 470 K for 15 min (to desorb residual water) and then equilibrated for 1 h. Variable temperature ^{1}H NMR spectra are shown in Figure 10. For the sample in air (Fig. 10a), two signals of H_2O_2 (δ_H = 12 ppm) and H_2O (δ_H = 5 ppm) are observed at $T < 240$ K. From the intensity ratio of these signals, and the temperature behavior of the 5 ppm signal (compared with pure water, Fig. 7a), one can assume that water includes a small portion of dissolved H_2O_2 (since bound

water is a poor solvent [17,44]). Similarly, the H_2O_2 structures responsible for the signal at 12 ppm are practically free of water. In other words, not only is bound water a poor, inactive solvent, but hydrogen peroxide is also.

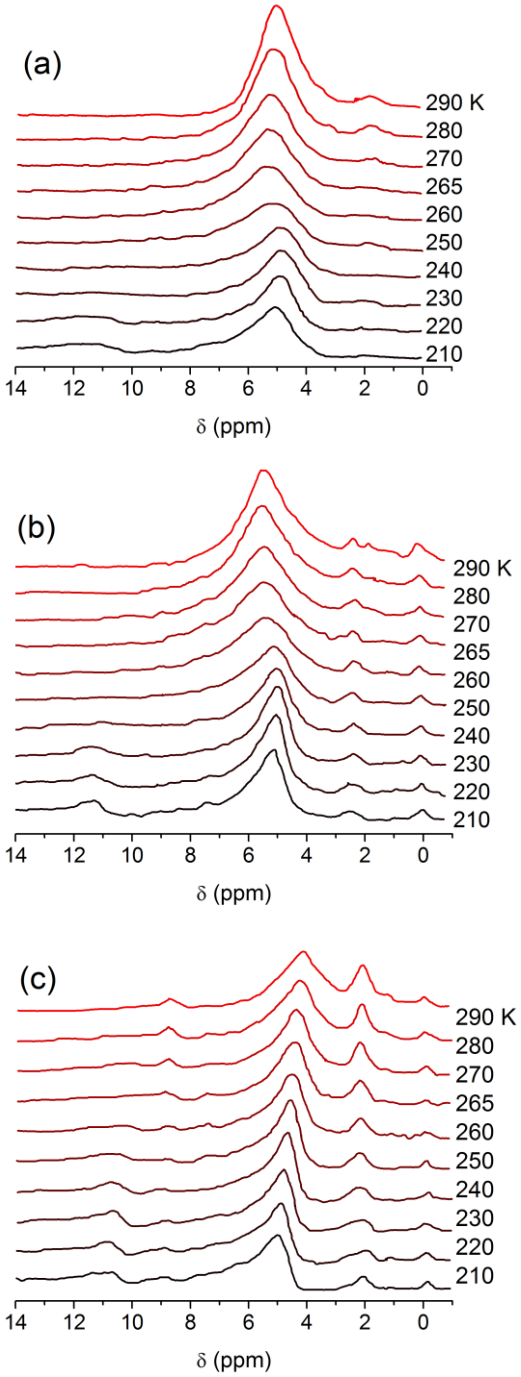

Fig. 10. ^{1}H NMR spectra of a solution of H_2O_2 (30%) in H_2O (70%) of 0.05 g per gram of dry silica CS20 in different dispersion media: (a) air, (b) chloroform-d, and (c) $CDCl_3/CD_3CN$ (mixture 8 : 1).

Thus, partial freezing of the solution and its cryoconcentration with decreasing temperature can cause the formation of spatially separated clusters (since proton exchange

between H_2O and H_2O_2 is slow on the NMR timescale [16,17]). At T > 240 K, the exchange becomes faster and the signal width of H_2O_2 becomes broader and, therefore, not detected (since the bandwidth is 20 kHz). The water resonance exhibits a slightly higher chemical shift due to the interaction of water with H_2O_2. Besides the signal of SAW at 5 ppm, a weak signal of WAW is observed at 1.8 ppm, the intensity of which increases with increasing temperature due to melting. The WAW does not interact with hydrogen peroxide because of space confined effects, and the formation of spatially separated structures with WAW and hydrogen peroxide occur.

In the $CDCl_3$ dispersion medium (Fig. 10b), ^1H NMR spectra are similar to those in air (Fig. 10a). However, the signal of WAW becomes more intense and less dependent on temperature. This suggests $CDCl_3$ slightly enhances clustering of the bound solution; however, the temperature behavior of SAW and H_2O_2 structures does not significantly change.

The addition of a small portion of polar CD_3CN to $CDCl_3$ leads to significant changes in the structure of the bound H_2O_2 solution (Fig. 10c). Signals of WAW and H_2O_2 increase and the latter appears as two temperature dependent signals at 11 and 9 ppm. CD_3CN is not found to dissolve in SAW. This is due to the low amount of water in the system causing a low water solvent activity [17]). This is evidenced by the fact that there is no change in SAW signal with and without CD_3CN. In addition there is no signal of complexes characteristic of $HO–H\cdots N{\equiv}CCD_3$ interactions, characterized by a resonance $\delta_H \approx 3.2$ ppm [17].

To study the interaction of concentrated (36%) hydrochloric acid with CS20, silica was dried at 420 K for 15 min, and then 0.1 g of the HCl solution per gram of dry silica was added (Fig. 11). In air (Fig. 11a), a single signal of the bound solution is observed; the chemical shift of which decreases from 9.5 ppm at 210 K to 8 ppm at 290 K. Spectra of the bound solution for the same sample in the chloroform-d medium are similar (Fig. 11b). On the left wing of the main signal, a signal of more concentrated solution of HCl in bound water is observed at a greater δ_H value. Additionally, a weak signal of WAW appears at 1.2 ppm due to clustering of bound water due to interaction with weakly polar $CDCl_3$.

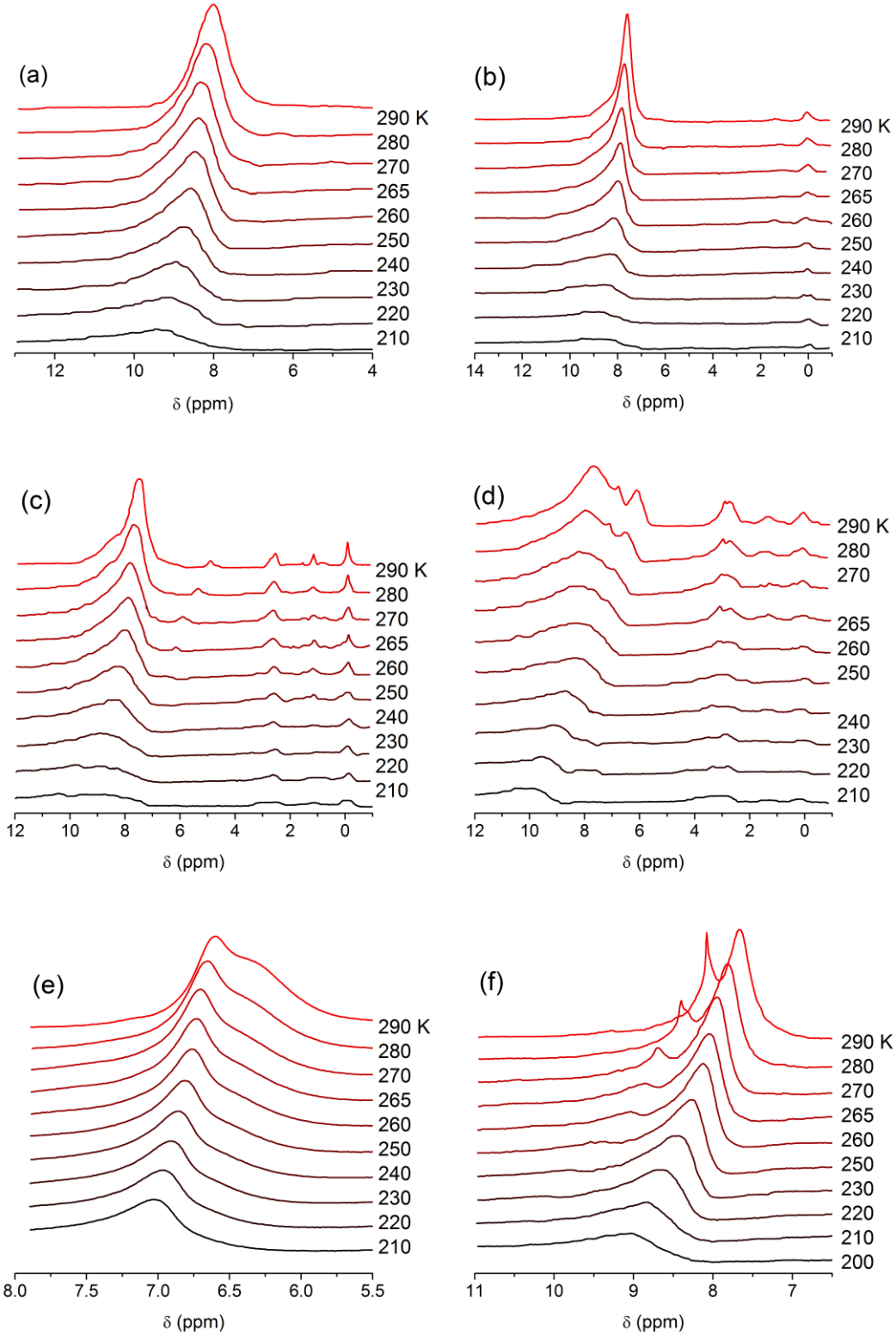

Fig. 11. ^{1}H NMR spectra of a solution of (a-e) HCl (36%) in H_2O (64%) of 0.1 g per gram of dry silica CS20 in different dispersion media: (a) air, (b) chloroform-d, (c, d) $CDCl_3/(CD_3)_2SO$ (mixture (c) 10 : 1 and (d) 10:2); (e) with addition of 0.08 g/g of water (in $CDCl_3$); and (f) water (0.1 g/g) in $CDCl_3/CF_3COOH$ (7:1).

After addition of DMSO-d_6 (Fig. 11c,d), the signal of structures from concentrated HCl increases. Additionally, the signal of structures with a smaller content of HCl is observed at $T >$

240 K. The spectra include signals of CH_3 groups of $(CH_3)_2SO$ (admixture in DMSO-d_6) at δ_H = 2.5 ppm, and WAW at δ_H = 1.2 ppm. With increasing content of DMSO-d_6 (Fig. 11d), intensity of the signal at 6-7 ppm assigned to domains with decreased HCl content, increases and splits into two resonances at T > 265 K. This result suggests the formation of domains with different dissolved HCl content. Thus, cryoconcentration effects depend on the dispersion medium composition. A decrease in the HCl concentration in the absence of polar co-solvents (Fig. 11e) results in differentiation of hydrochloric acid/water structures in the chloroform medium.

Variations in the temperature dependence of water domain clustering are observed for water bound to CS20 placed in the $CDCl_3$/TFAA (trifluoroacetic acid) dispersion medium (Fig. 11f). In this case, the signal of domains with more concentrated acid solution (characterized by downfield signal at δ_H = 8-9 ppm) is weaker than the main (right) signal at 7.5-8.5 ppm at T > 250 K (Fig. 11f).

The behavior of water bound to CS20m ($h \approx 100$ mg/g) was also analyzed depending on storage of the sample under different conditions (Fig. 12). The sample CS20m stored at 255 K for a week was loaded into cooled NMR ampoule, and after the NMR spectra recording, this sample was stored at 293 K for a week in air, and the spectra were recorded again (Fig 12). A small difference in the spectra (Fig. 12a) and the $C_{uw}(T)$ curves (Fig. 12b) can be caused by adsorption of an additional portion of water from air onto the cooled sample. This results in an increase in the signal intensity. Adsorbed water is located in narrow voids mainly at R < 3 nm (Fig. 12c). Therefore, the surface area of silicas in contact with bound water is about 40 m^2/g (Table 2, S_{uw}), and $S_{nano} > S_{meso}$; however, $V_{nano} < V_{meso}$. Therefore, the major portion of water (~80%) is strongly bound water (Table 2, C_{uw}^{s}). This leads to the $\gamma_S^* = \gamma_S/h$ value recalculated per gram of water (~80 J/g) greater than that for the aqueous suspension but lower than that for a sample in the methane atmosphere. As a whole, the observed changes in the behavior of water bound to CS20m stored under different conditions are small (Fig. 12) due to the stability of cryosilica properties.

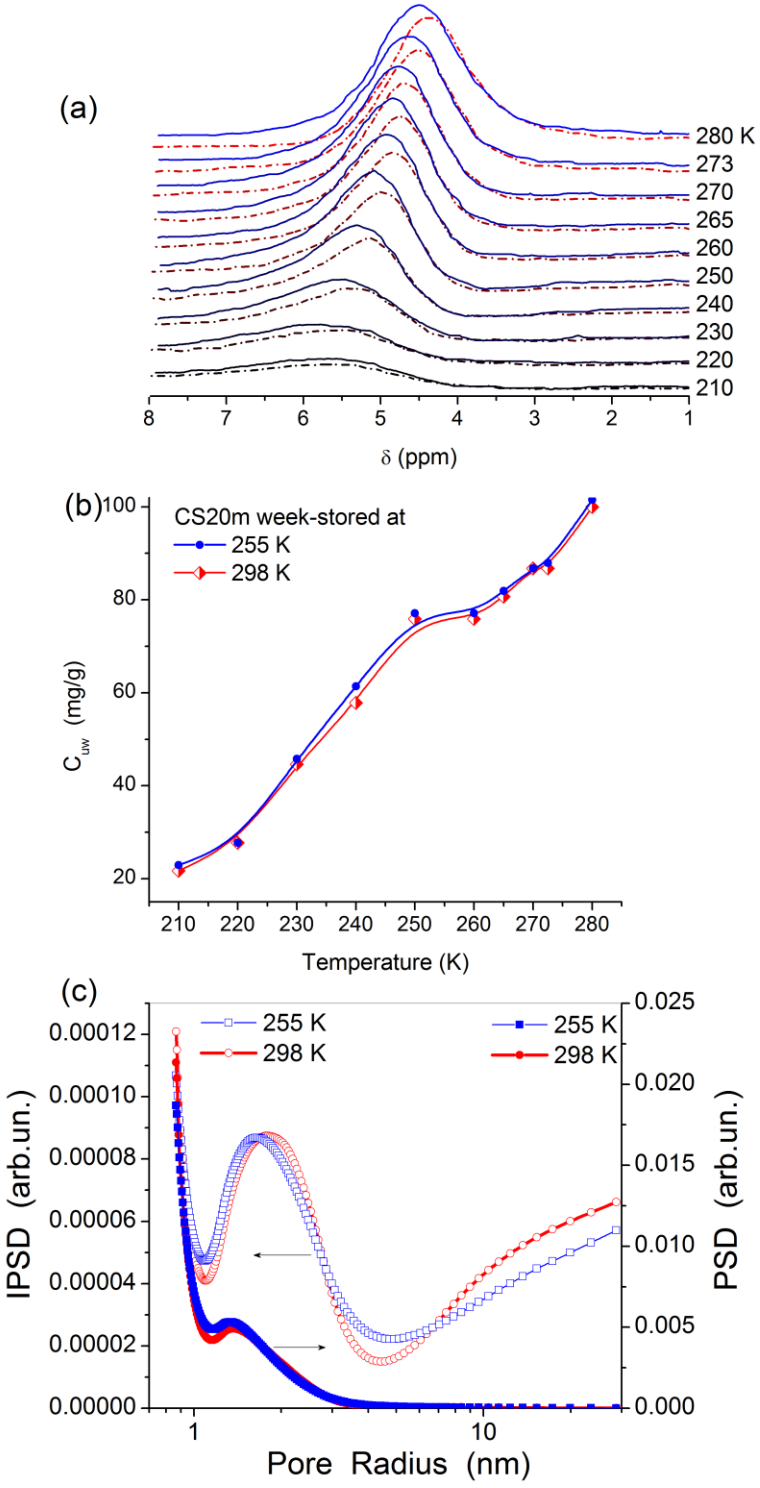

Fig. 12. (a) ^{1}HMR spectra of CS20m stored at 255 K (solid lines) for a week and then stored at 298 K (dashed lines) for a week; and the corresponding (b) $C_{uw}(T)$ dependences and (c) PSD and IPSD.

This aspect is of importance because silica samples were studied using a set of methods under very different conditions including TSDC measurements of strongly cooled samples (Fig. 13).

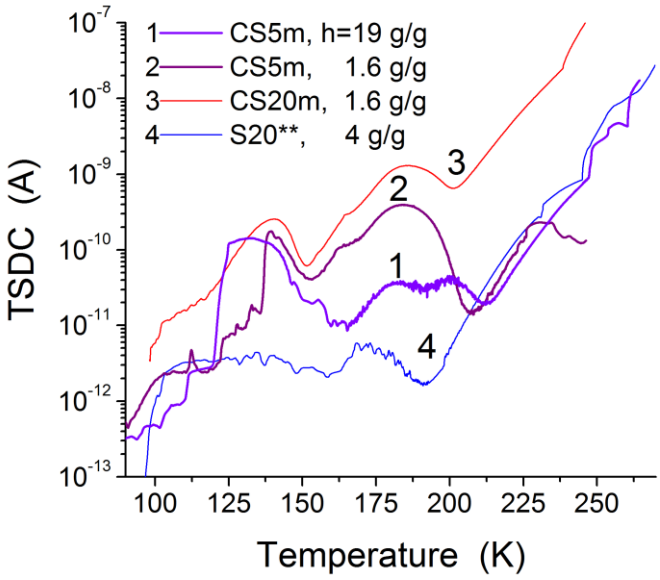

Fig. 13. TSDC thermograms (normalized to F_p = 100 V/mm) of cryosilicas CS5 and CS20m dried and hydrated at h = 1.6 g/g, thawed aqueous suspension of CS5m (1000 atm) and gel-like concentrated suspension (S20**, 20 wt% of A-300) prepared at standard condition without freezing.

TSDC thermograms show dipolar relaxations at T < 220-220 K and direct current (dc) relaxation at T > 210-220 K (Fig. 13). In contrast to ^{1}H NMR showing nonzero intensity due to local mobility of molecules, the dc relaxation is due to through conductivity when there are conditions for percolation of protons or $H_3O^+(H_2O)_n$ (i.e. Eigen and Zundel cations) between two electrodes [29]. Therefore, the dc relaxation can start at slightly higher temperatures than the NMR spectra appear for mobile molecules of adsorbates. The activation energy (assuming that the dc relaxation obeys the Arrhenius law) is relatively low for the system studied (54.8, 52.7, 41.3 and 55.2 kJ/mol for curves 1-4, Fig. 13, respectively). The E_a value for the CS5 suspension is smaller than that for initial 5 wt.% aqueous suspension of nanosilica [17,29].

The TSDC is higher for wetted powder of CS20m (h = 1.6 g/g) than for other samples (Fig. 13) because the relative amount of water contacted with the silica surface is greater than in other samples. The high-pressure cryogelation effects appear since the TSDC intensity is much lower for 20 wt.% suspension of A-300 (nontreated at low temperature and only sonicated) than that of not only for CS20m but also for CS5m. The TSDC intensity for dipolar relaxations increases with increasing silica content from 5 wt.% to 20 wt.% for cryosilicas because water

molecules are strongly polarized by the electrostatic fields near the silica surface. However, this effect depends also on the organization of silica nanoparticles in secondary structures.

2. Conclusion

High-pressure cryogelation affects the properties of cryosilica powders and suspensions depending on the silica content in initial aqueous suspensions (5-20 wt.%) frozen-dried. The largest changes are observed for CS20 and CS20m (20 wt.% suspension frozen at 450 or 1000 atm, respectively). For instance, adsorption of water onto CS20 from air increases several-fold in comparison with CS5, CS10 or CS15. The specific surface area decreases slightly during high-pressure cryogelation. This is due to rearrangement of primary nanoparticles in the secondary structures, which are denser than the initial silica powder. However, the structure of primary particles *per se* changes only slightly according to HRTEM images. This rearrangement results in changes of the PSD shape and contributions of pores of different shapes (cylindrical, slit-shaped, and voids between nanoparticles) and sizes (nano-, meso-, and macropores).

Low-temperature (200-290 K) ^{1}H NMR spectroscopy investigations of water adsorbed alone, or co-adsorbed with small amounts of hydrogen peroxide, hydrochloric acid or trifluoroacetic acid probe the temperature dependence of cryoconcentration and clustering of liquid co-adsorbates. NMR cryoporometry, TG thermoporometry and TSDC thermograms show changes in the organization of interfacial water and other co-adsorbates depending on temperature, concentration, and dispersion medium type. In general, all liquids bound in small amounts to silicas are poor solvents compared to bulk liquids.

Thus, high-pressure cryogelation of oxides (as well as polymers) provides additional ways to change the textural, structural, morphological, and adsorption characteristics of the materials.

References

[1] B. Mattiasson, A. Kumar, I.Yu. Galaev (Eds.), Macroporous Polymers. Production Properties and Biotechnological/Biomedical Applications, CRC Press, London, New York, 2009.

[2] Z.F. Cui (Ed.), Medical Biothechnology and Health Care, Vol. 5, Second edn., Elsevier, Oxford, 2011.

[3] P. Dubruel, R. Unger, S. Van Vlierberghe, V. Cnudde, P.J.S. Jacobs, E. Schacht, C.J. Kirkpatrick, Porous gelatin hydrogels: 2. In vitro cell interaction study, Biomacromolecules 8 (2007) 338-344.

[4] E.L. Hedberg, C.K. Shih, J.J. Lemoine, M.D. Timmer, M.A. Liebschner, J.A. Jansen, A.G. Mikos, In vitro degradation of porous poly(propylene fumarate)/poly(DL-lactic-co-glycolic acid) composite scaffolds, Biomaterials 26 (2005) 3215-3225.

[5] V.M. Gun'ko, I.N. Savina, S.V. Mikhalovsky, Cryogels: morphological, structural and adsorption characterisation, Adv. Colloid Interface Sci. 187–188 (2013) 1–46.

[6] Sh.R. Mukai, H. Nishihara, S. Shichi, H. Tamon, Preparation of porous TiO_2 cryogel fibers through unidirectional freezing of hydrogel followed by freeze-drying, Chem. Mater. 16 (2004) 4987-4991.

[7] A. Pons, Ll. Casas, E. Estop, E. Molins, K.D.M. Harris, M. Xu, A new route to aerogels: Monolithic silica cryogels, J. Non-Crystal. Solid 358 (2012) 461-469.

[8] H. Nishihara, S.R. Mukai, S. Shichi, H. Tamon, Preparation of titania–silica cryogels with controlled shapes and photocatalysis through unidirectional freezing, Materials Letters 64 (2010) 959–961.

[9] H. Tamon, T. Akatsuka, H. Mori, N. Sano, Synthesis of zeolite monolith with hierarchical micro/macropores by ice-templating and steam-assisted crystallization, Chem. Eng. Trans. 32 (2013) 2059-2064.

[10] B. Babić, M. Kokunešoski, M. Miljković, M. Prekajski, B. Matović, J. Gulicovski, D. Bučevac, Synthesis and characterization of the SBA-15/carbon cryogel nanocomposites, Ceramic Int. 38 (2012) 4875-4883.

[11] Z.M. Marković, B.M. Babić, M.D. Dramićanin, I.D. Holclajtner Antunović, V.B. Pavlović, D.B. Peruško, B.M. Todorović Marković, Preparation of highly conductive carbon cryogel based on pristine graphene, Synthetic Metals 162 (2012) 743-747.

[12] G. Amaral-Labat, A. Szczurek, V. Fierro, N. Stein, C. Boulanger, A. Pizzi, A. Celzard, Pore structure and electrochemical performances of tannin-based carbon cryogels, Biomass Bioenergy 39 (2012) 274-282.

[13] V.V. Babkov, V.N. Mokhov, S.M. Kapitonov, P.G. Komokhov, Structure formation and disintegration of cement concretes, Ufa, Ufa Polygraphkombinat, 2002 (in Russian).

[14] A. Mills, The freezing bomb, Phys. Education 45 (2010) 153-157.

[15] A.L. Vidovskii, Experimental determination of pressure during ice expansion, Hydrotechnical Construction 6 (1972) 791-792.

[16] V.M. Gun'ko, V.V. Turov, V.M. Bogatyrev, V.I. Zarko, R. Leboda, E.V. Goncharuk, A.A. Novza, A.V. Turov, A.A. Chuiko, Unusual properties of water at hydrophilic/hydrophobic interfaces, Adv. Colloid Interface Sci. 118 (2005) 125-172.

[17] V.M. Gun'ko, V.V. Turov, Nuclear Magnetic Resonance Studies of Interfacial Phenomena, CRC Press, Boca Raton, 2013.

[18] V.P. Glushko (Ed.), Handbook of Thermodynamic Properties of Individual Substances, Nauka, Moscow, 1978 (in Russian).

[19] J. Mitchell, J.B.W. Webber, J.H. Strange, Nuclear magnetic resonance cryoporometry, Phys. Rep. 461 (2008) 1-36.

[20] O. V. Petrov, I. Furó, NMR cryoporometry: Principles, application and potential, Progr. NMR Spectroscopy 54 (2009) 97-122.

[21] D.W. Aksnes, K. Forl, L. Kimtys, Pore size distribution in mesoporous materials as studied by ^{1}H NMR, Phys. Chem. Chem. Phys. 3 (2001) 3203-3207.

[22] J.B.W. Webber, R. Anderson, J.H. Strange, B. Tohidi, Clathrate formation and dissociation in vapor/water/ice/hydrate systems in SBA-15, sol–gel and CPG porous media, as probed by NMR relaxation, novel protocol NMR cryoporometry, neutron scattering and *ab initio* quantum–mechanical molecular dynamics simulation, Magnet. Reson. Imag. 25 (2007) 533–536.

[23] S. Brunauer, P. H. Emmett, E. Teller, Adsorption of gases in multimolecular layers, J. Am. Chem. Soc. 60 (1938) 309-319.

[24] S.J. Gregg, K.S.W. Sing, Adsorption, Surface Area and Porosity, Academic Press, London, 1982.

[25] V.M. Gun'ko, Consideration of the multicomponent nature of adsorbents during analysis of their structural and energy parameters, Theoret. Experim. Chem. 36 (2000) 319-324.

[26] V.M. Gun'ko, R. Leboda, J. Skubiszewska-Zięba, Heating effects on morphological and textural characteristics of individual and composite nanooxides, Adsorption 15 (2009) 89-98.

[27] V.M. Gun'ko, S.V. Mikhalovsky, Evaluation of slitlike porosity of carbon adsorbents, Carbon 42 (2004) 843-849.

[28] J. Goworek, W. Stefaniak, W. Zgrajka, Measuring porosity of polymeric adsorbents by temperature programmed desorption of liquids, Mater. Chem. Phys. 59 (1999) 149-153.

[29] V.M. Gun'ko, V.I. Zarko, E.V. Goncharuk, L.S. Andriyko, V.V. Turov, Y.M. Nychiporuk, R. Leboda, J. Skubiszewska-Zięba, A.L. Gabchak, V.D. Osovskii, Y.G. Ptushinskii, G.R. Yurchenko, O.A. Mishchuk, P.P. Gorbik, P. Pissis, J.P. Blitz, TSDC spectroscopy of relaxational and interfacial phenomena, Adv. Colloid Interface Sci. 131 (2007) 1-89.

[30] C.J. Brinker, G.W. Scherer, Sol-Gel Science: The Physics and Chemistry of Sol-Gel Processing, Academic Press, New York, 1990.

[31] A.C. Pierre, Introduction to Sol-Gel Processing, Kluwer, Boston, 1998.

[32] Basic Characteristics of Aerosil. Technical Bulletin Pigments, No 11, Degussa AG, Hanau, 1997.

[33] R.K. Iler, The Chemistry of Silica, Wiley, Chichester, 1979.

[34] A.P. Legrand, (Ed.), The Surface Properties of Silicas, Wiley, New York, 1998.

[35] E.F. Vansant, P. Van Der Voort, K.C. Vrancken, Characterization and Chemical Modification of the Silica Surface: Studies in Surface Science and Catalysis Vol. 93, Elsevier, Amsterdam, 1995.

[36] A.V. Kiselev, V.I. Lygin, Infrared Spectra of Surface Compounds, Wiley, New York, 1975.

[37] V.M. Gun'ko, J. Skubiszewska-Zięba, R. Leboda, K.N. Khomenko, O.A. Kazakova, M.O. Povazhnyak, I.F. Mironyuk, Influence of morphology and composition of fumed oxides on changes in their structural and adsorptive characteristics on hydrothermal treatment at different temperatures, J. Colloid Interface Sci. 269 (2004) 403-424.

[38] V.M. Gun'ko, E.F. Voronin, I. F. Mironyuk, R. Leboda, J. Skubiszewska-Zięba, E.M.Pakhlov, N.V. Guzenko, A.A. Chuiko, The effect of heat, adsorption and mechanochemical treatments on stuck structure and adsorption properties of fumed silicas, Colloids Surf. A: Physicochem. Eng. Aspects 218 (2003) 125–135.

[39] V.M. Gun'ko, V.I. Zarko, E.F. Voronin, V.V. Turov, I.F. Mironyuk, I.I. Gerashchenko, E.V. Goncharuk, E.M. Pakhlov, N.V. Guzenko, R. Leboda, J. Skubiszewska-Zięba, W. Janusz, S. Chibowski, Yu.N. Levchuk, A.V. Klyueva, Impact of some organics on structural and adsorptive characteristics of fumed silica in different media, Langmuir 18 (2002) 581-596.

[40] I.F. Mironyuk, V.M. Gun'ko, V.V. Turov, V.I. Zarko, R. Leboda, J. Skubiszewska-Zięba, Characterization of fumed silicas and their interaction with water and dissolved proteins, Colloids Surf. A: Physicochem. Eng. Aspects 180 (2001) 87-101.

[41] V.M. Gun'ko, I.F. Mironyuk, V.I. Zarko, V.V. Turov, E.F. Voronin, E.M. Pakhlov, E.V. Goncharuk, R. Leboda, J. Skubiszewska-Zięba, W. Janusz, S. Chibowski, Yu.N. Levchuk, A.V. Klyueva, Fumed Silicas possessing different morphology and hydrophilicity, J. Colloid Interface Sci. 242 (2001) 90-103.

[42] Fiji is just ImageJ, http://fiji.sc/Fiji.

[43] A.A. Chuiko (Ed.), Chemistry of Silica Surface, UkrINTEI, Kiev, 2001 (in Russian).

[44] M. Chaplin, Water Structure and Science, http://www.lsbu.ac.uk/water/, April 3, 2013.

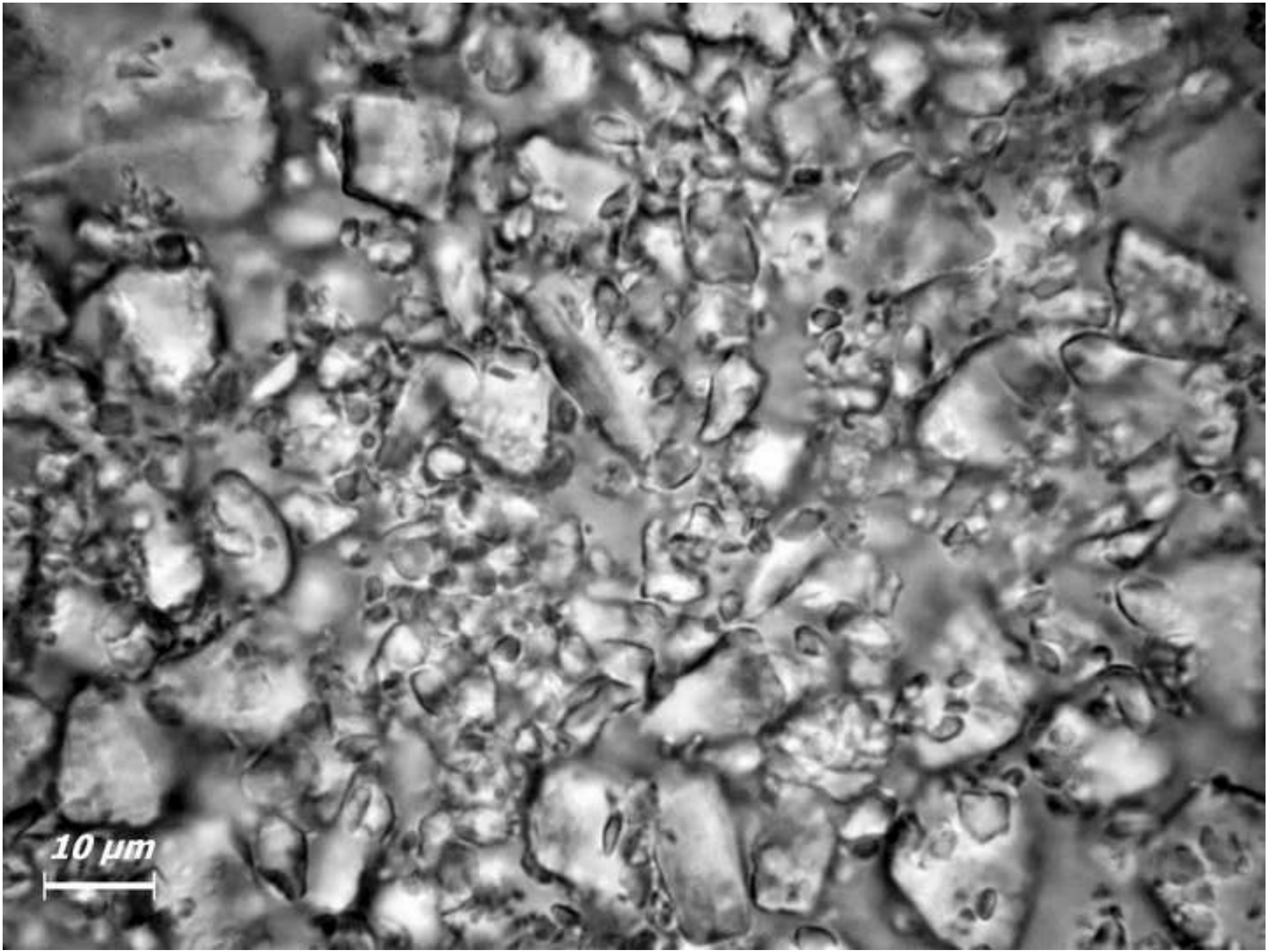

Figure 1

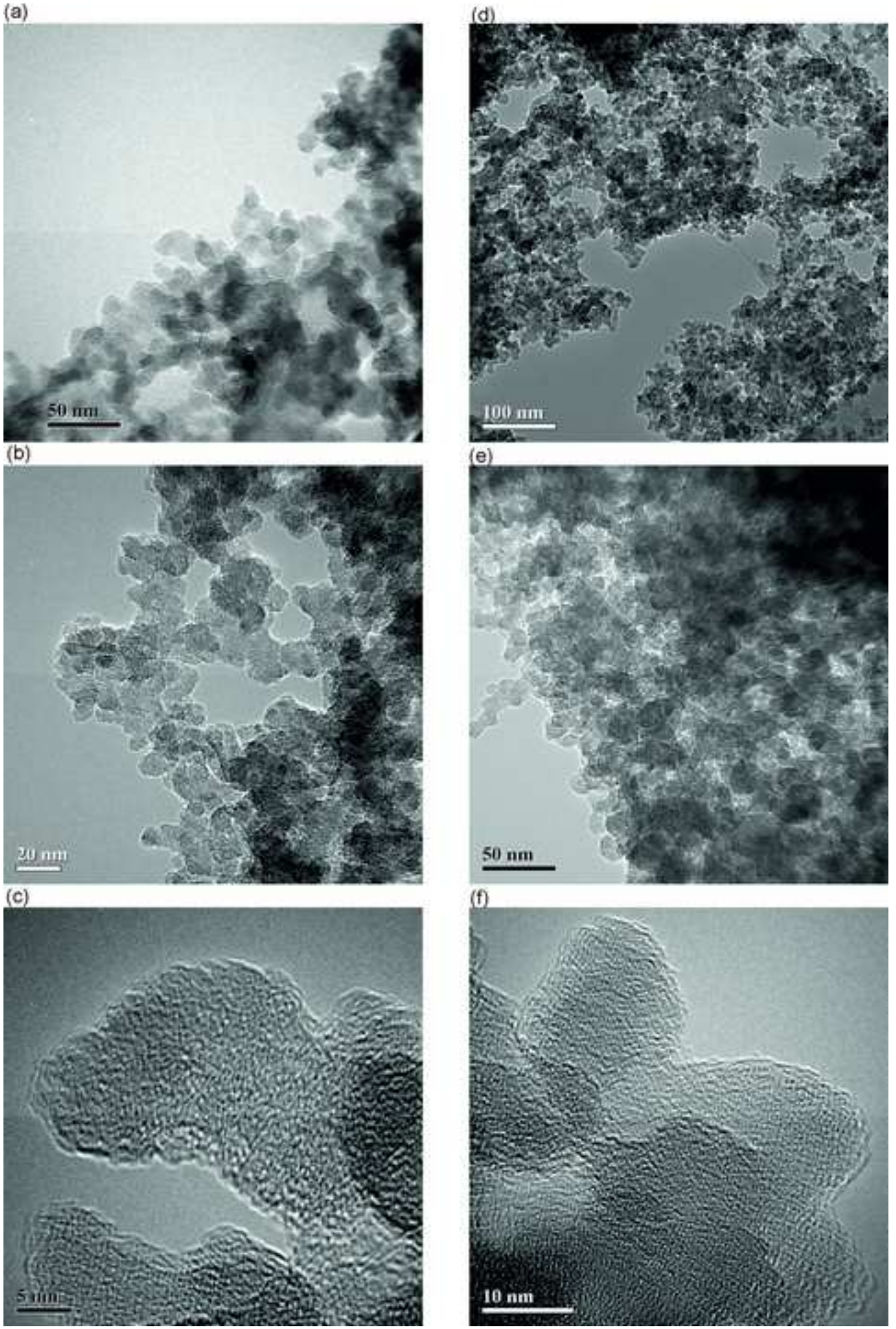

Figure 2

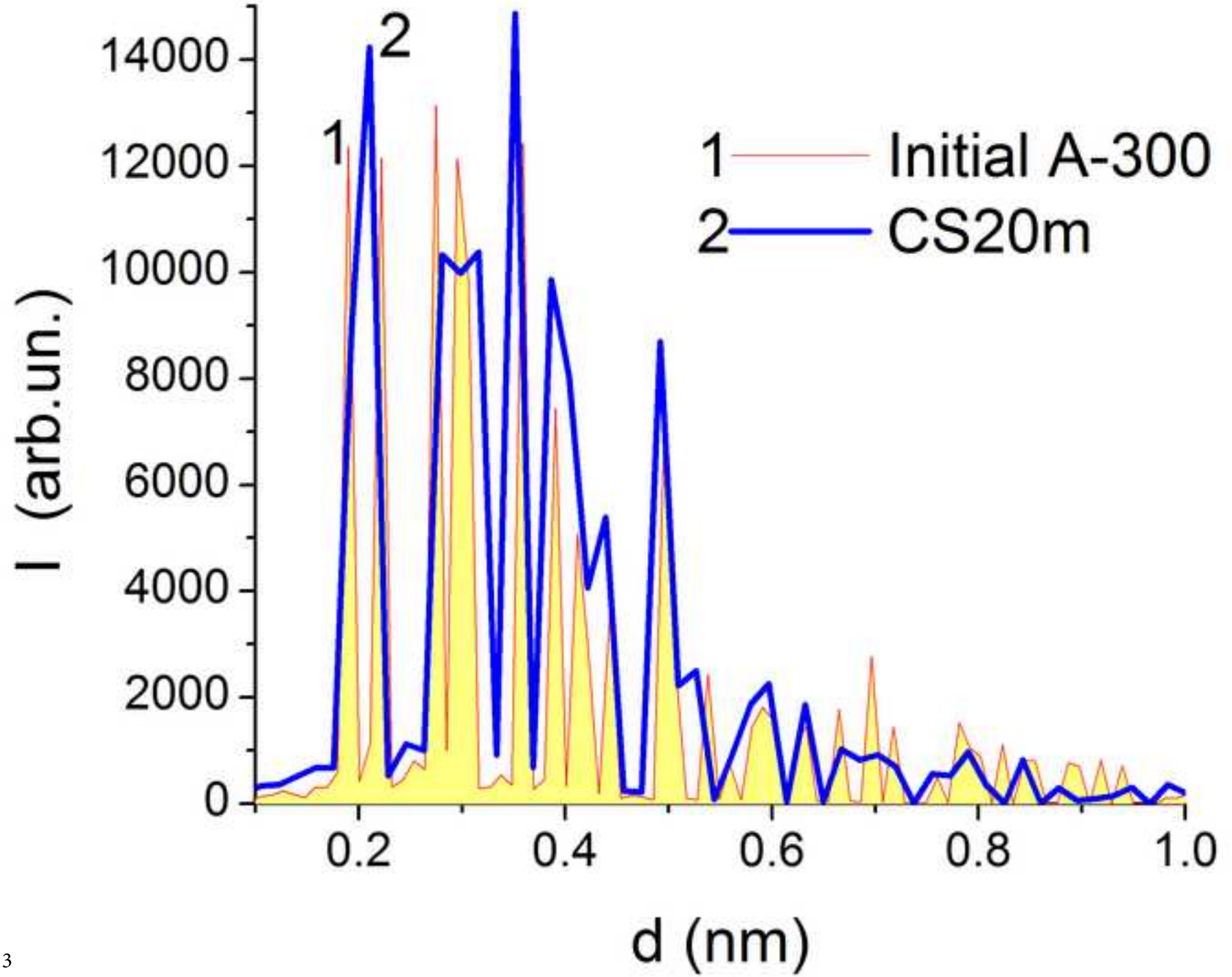
14000
12000
10000
8000
6000
4000
2000
0
I (arb.un.)
0.2
0.4
0.6
0.8
1.0
d (nm)
1
2
1 Initial A-300
2 CS20m

Fugure 3

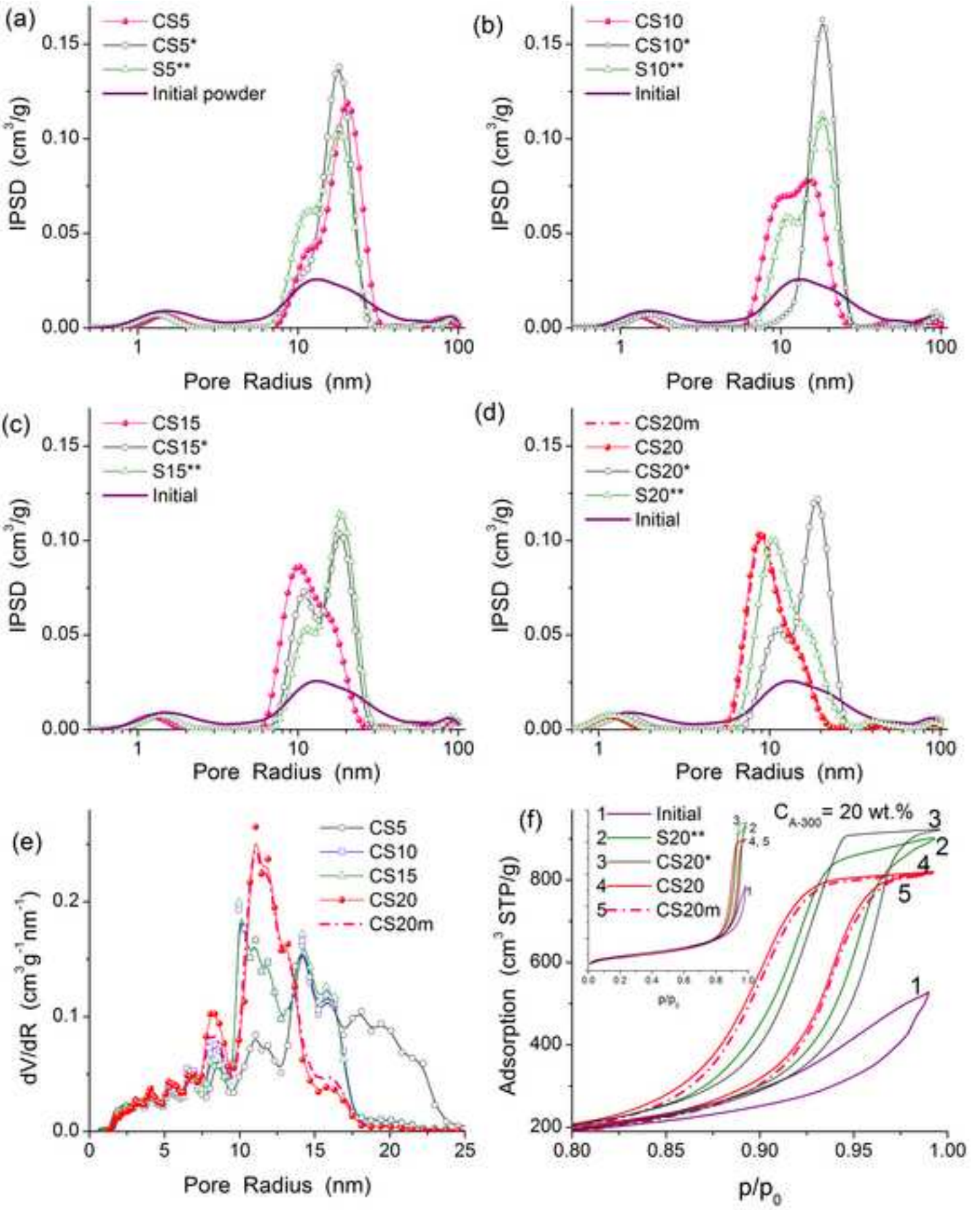
(a)
CS5
CS5*
S5**
Initial powder
IPSD (cm³/g)
Pore Radius (nm)
(b)
CS10
CS10*
S10**
Initial
(c)
CS15
CS15*
S15**
Initial
(d)
CS20m
CS20
CS20*
S20**
Initial
(e)
CS5
CS10
CS15
CS20
CS20m
dV/dR (cm³g⁻¹nm⁻¹)
(f)
1 Initial
2 S20**
3 CS20*
4 CS20
5 CS20m
C A-300 = 20 wt.%
Adsorption (cm³ STP/g)
p/p0

Figure 4

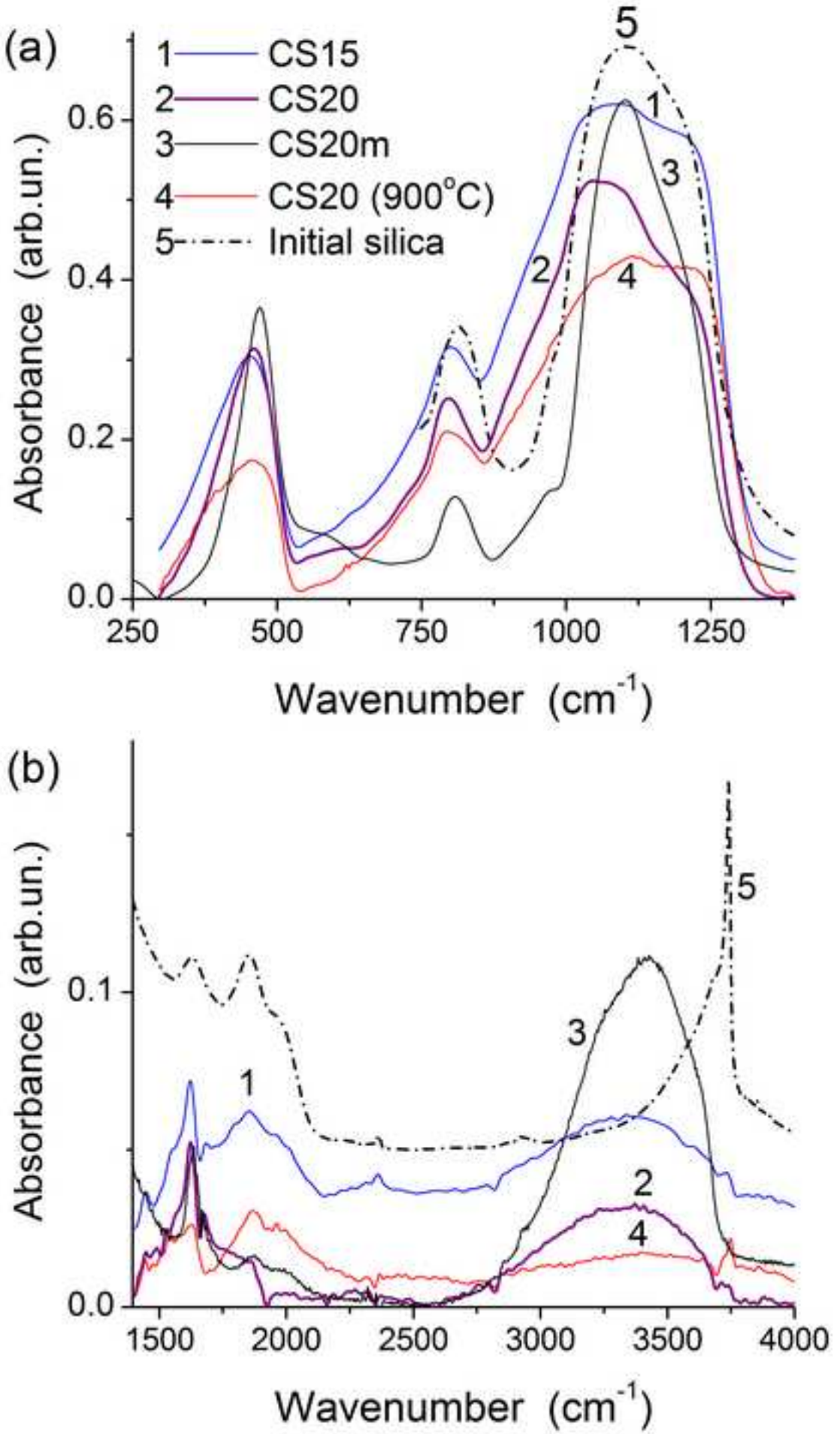
(a)
1 CS15
2 CS20
3 CS20m
4 CS20 (900°C)
5 Initial silica
Absorbance (arb.un.)
0.0
0.2
0.4
0.6
250
500
750
1000
1250
Wavenumber (cm-1)
(b)
Absorbance (arb.un.)
0.0
0.1
1500
2000
2500
3000
3500
4000
Wavenumber (cm-1)

Figure 5

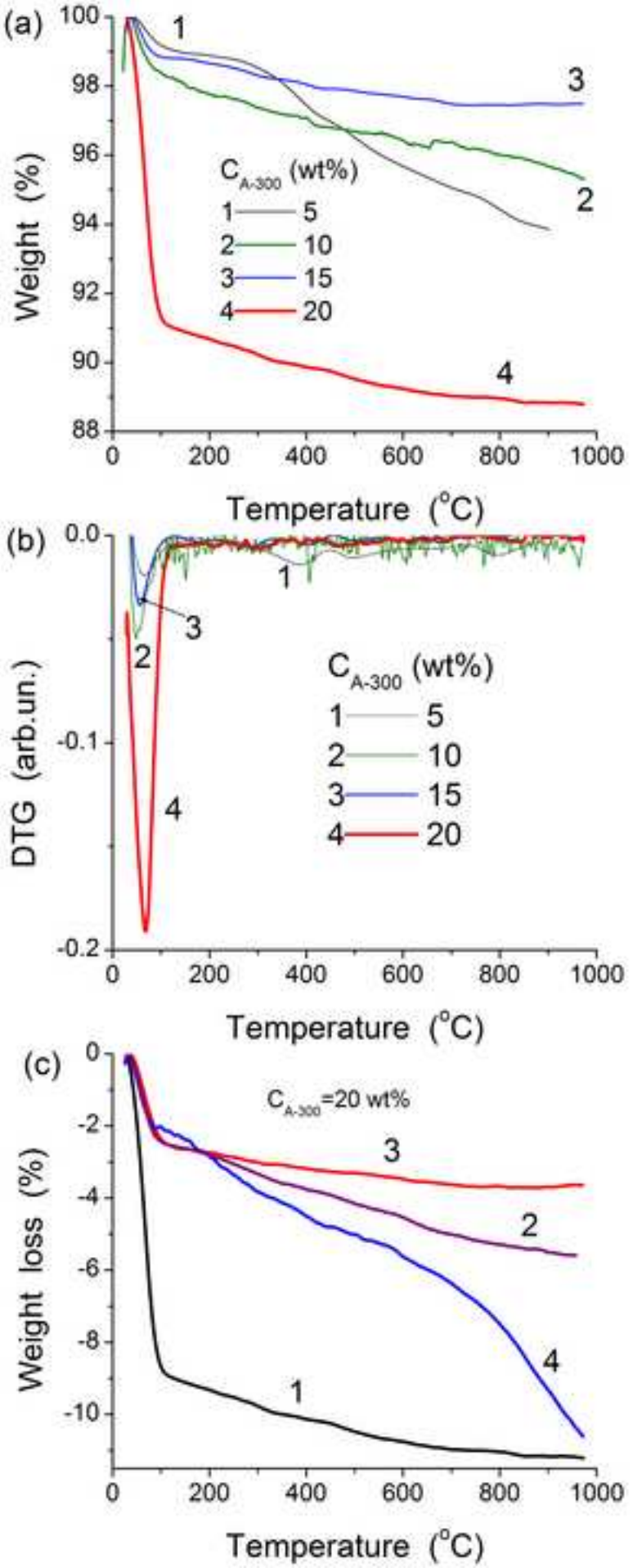
(a)
Weight (%)
Temperature (°C)
C A-300 (wt%)
1 5
2 10
3 15
4 20
(b)
DTG (arb.un.)
Temperature (°C)
(c)
Weight loss (%)
C A-300=20 wt%
Temperature (°C)

Figure 6

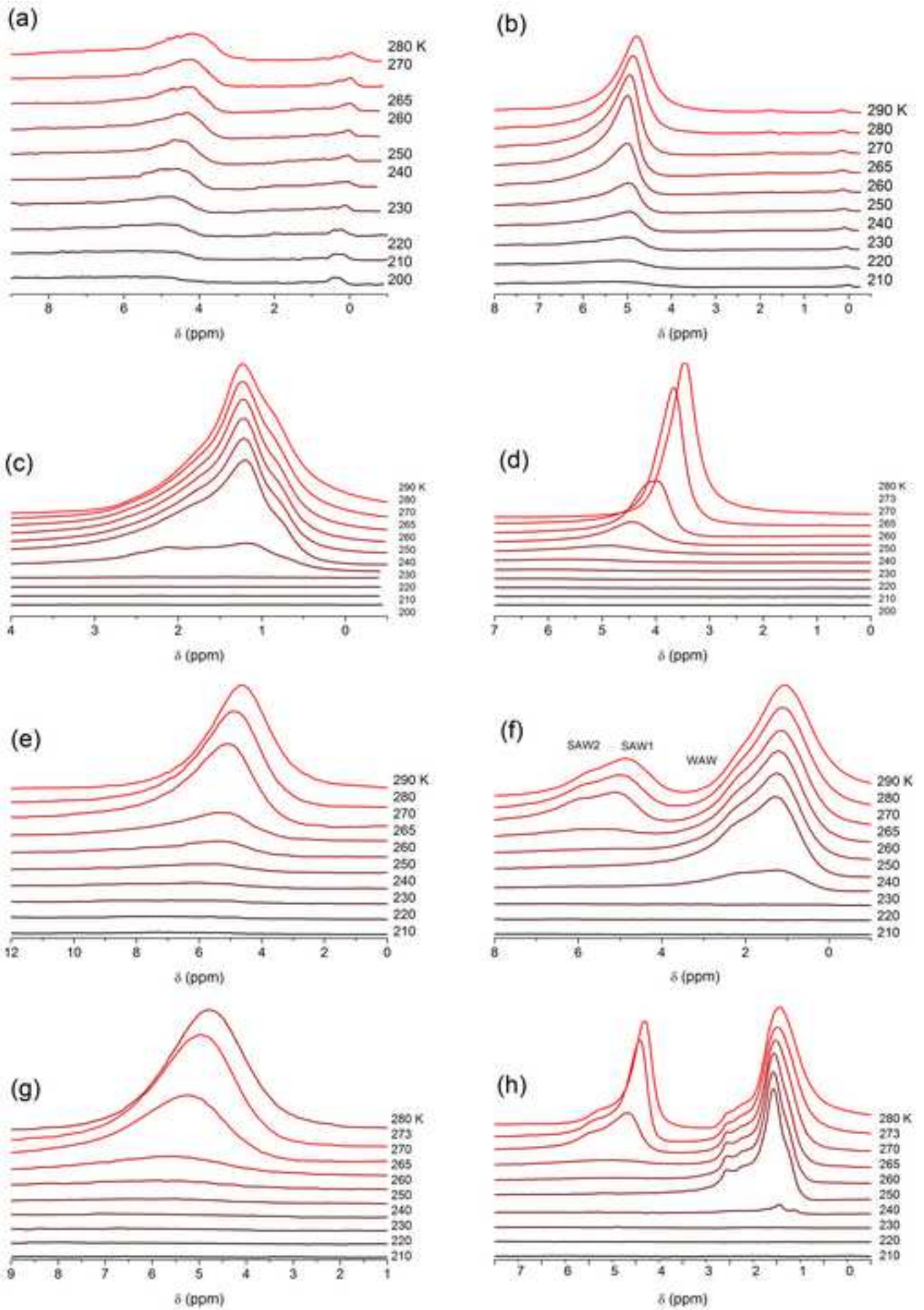
(a)
280 K
270
265
260
250
240
230
220
210
200
δ (ppm)
(b)
290 K
280
270
265
260
250
240
230
220
210
δ (ppm)
(c)
δ (ppm)
(d)
δ (ppm)
(e)
290 K
280
270
265
260
250
240
230
220
210
δ (ppm)
(f)
SAW2
SAW1
WAW
290 K
280
270
265
260
250
240
230
220
210
δ (ppm)
(g)
280 K
273
270
265
260
250
240
230
220
210
δ (ppm)
(h)
280 K
273
270
265
260
250
240
230
220
210
δ (ppm)

Figure 7

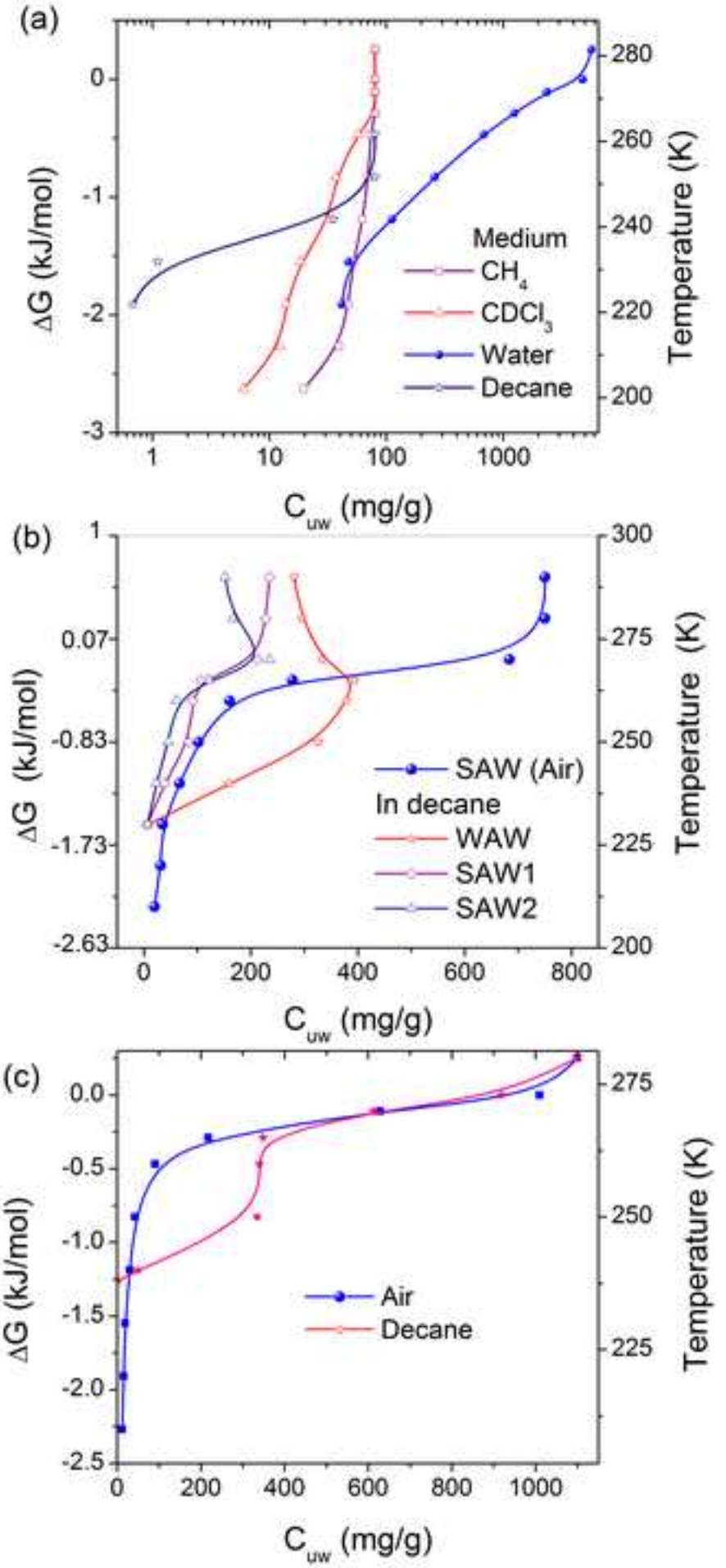
(a)
ΔG (kJ/mol)
Temperature (K)
C_uw (mg/g)
Medium
CH4
CDCl3
Water
Decane
(b)
ΔG (kJ/mol)
Temperature (K)
C_uw (mg/g)
SAW (Air)
In decane
WAW
SAW1
SAW2
(c)
ΔG (kJ/mol)
Temperature (K)
C_uw (mg/g)
Air
Decane

Figure 8

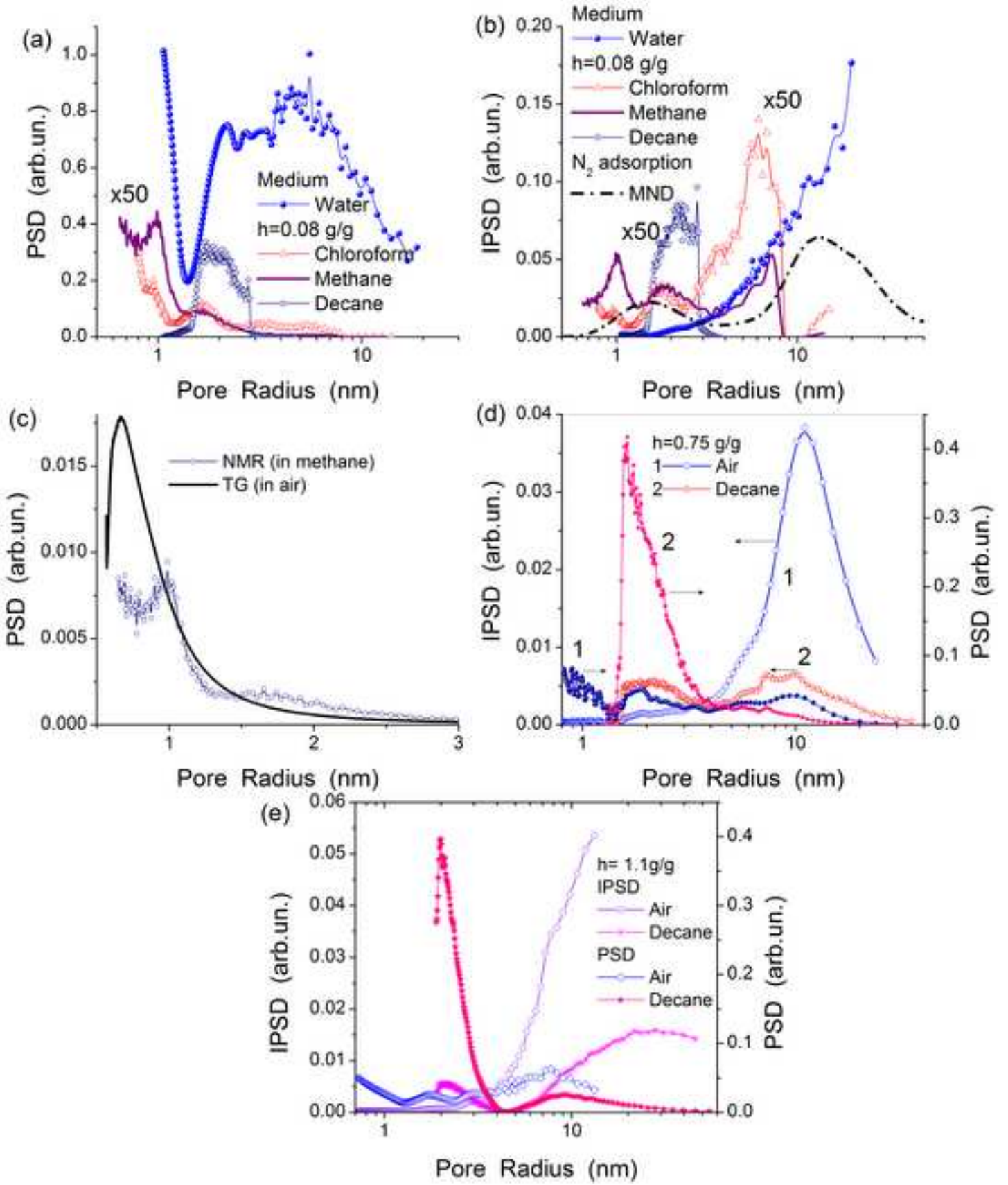
(a)
PSD (arb.un.)
x50
Medium
Water
h=0.08 g/g
Chloroform
Methane
Decane
Pore Radius (nm)
(b)
IPSD (arb.un.)
Medium
Water
h=0.08 g/g
Chloroform
Methane
Decane
N2 adsorption
MND
x50
x50
Pore Radius (nm)
(c)
PSD (arb.un.)
NMR (in methane)
TG (in air)
Pore Radius (nm)
(d)
IPSD (arb.un.)
PSD (arb.un.)
h=0.75 g/g
1 Air
2 Decane
1
2
1
2
Pore Radius (nm)
(e)
IPSD (arb.un.)
PSD (arb.un.)
h= 1.1g/g
IPSD
Air
Decane
PSD
Air
Decane
Pore Radius (nm)

Figure 9

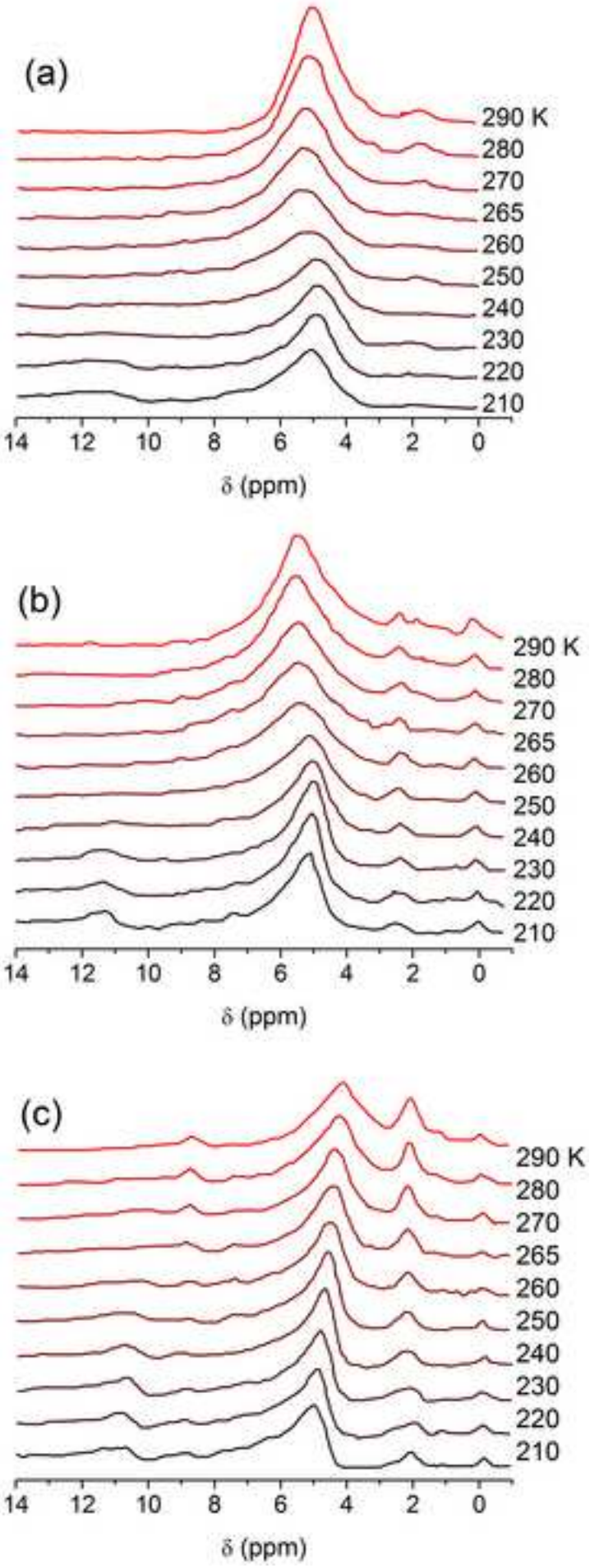
(a)
290 K
280
270
265
260
250
240
230
220
210
14 12 10 8 6 4 2 0
δ (ppm)
(b)
290 K
280
270
265
260
250
240
230
220
210
14 12 10 8 6 4 2 0
δ (ppm)
(c)
290 K
280
270
265
260
250
240
230
220
210
14 12 10 8 6 4 2 0
δ (ppm)

Figure 10

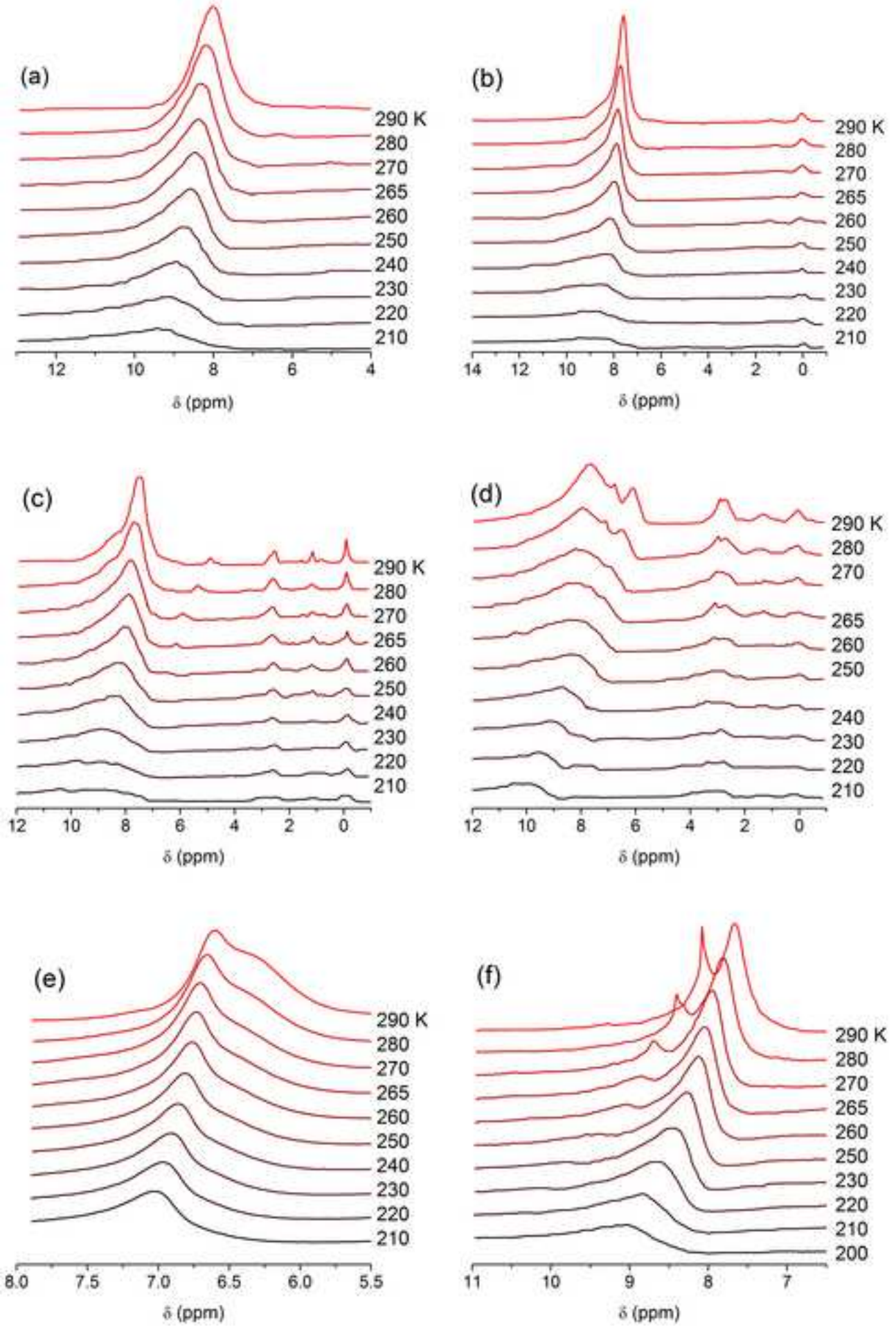
(a)
290 K
280
270
265
260
250
240
230
220
210
12
10
8
6
4
δ (ppm)
(b)
290 K
280
270
265
260
250
240
230
220
210
14
12
10
8
6
4
2
0
δ (ppm)
(c)
290 K
280
270
265
260
250
240
230
220
210
12
10
8
6
4
2
0
δ (ppm)
(d)
290 K
280
270
265
260
250
240
230
220
210
12
10
8
6
4
2
0
δ (ppm)
(e)
290 K
280
270
265
260
250
240
230
220
210
8.0
7.5
7.0
6.5
6.0
5.5
δ (ppm)
(f)
290 K
280
270
265
260
250
230
220
210
200
11
10
9
8
7
δ (ppm)

Figure 11

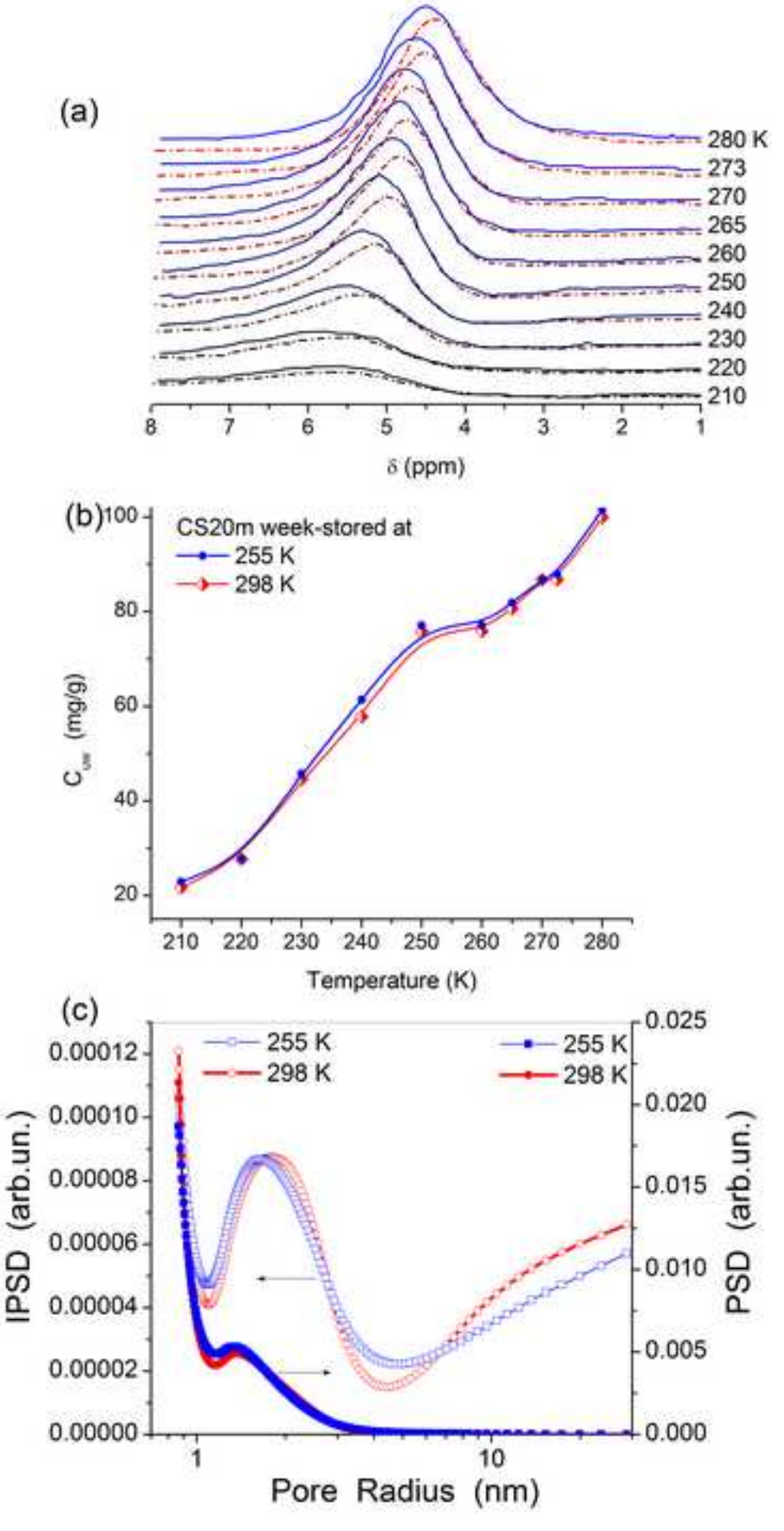
(a)
280 K
273
270
265
260
250
240
230
220
210
8
7
6
5
4
3
2
1
δ (ppm)
(b)
CS20m week-stored at
255 K
298 K
100
80
60
40
20
C_ue (mg/g)
210
220
230
240
250
260
270
280
Temperature (K)
(c)
255 K
298 K
255 K
298 K
0.00012
0.00010
0.00008
0.00006
0.00004
0.00002
0.00000
IPSD (arb.un.)
0.025
0.020
0.015
0.010
0.005
0.000
PSD (arb.un.)
1
10
Pore Radius (nm)

Figure 12

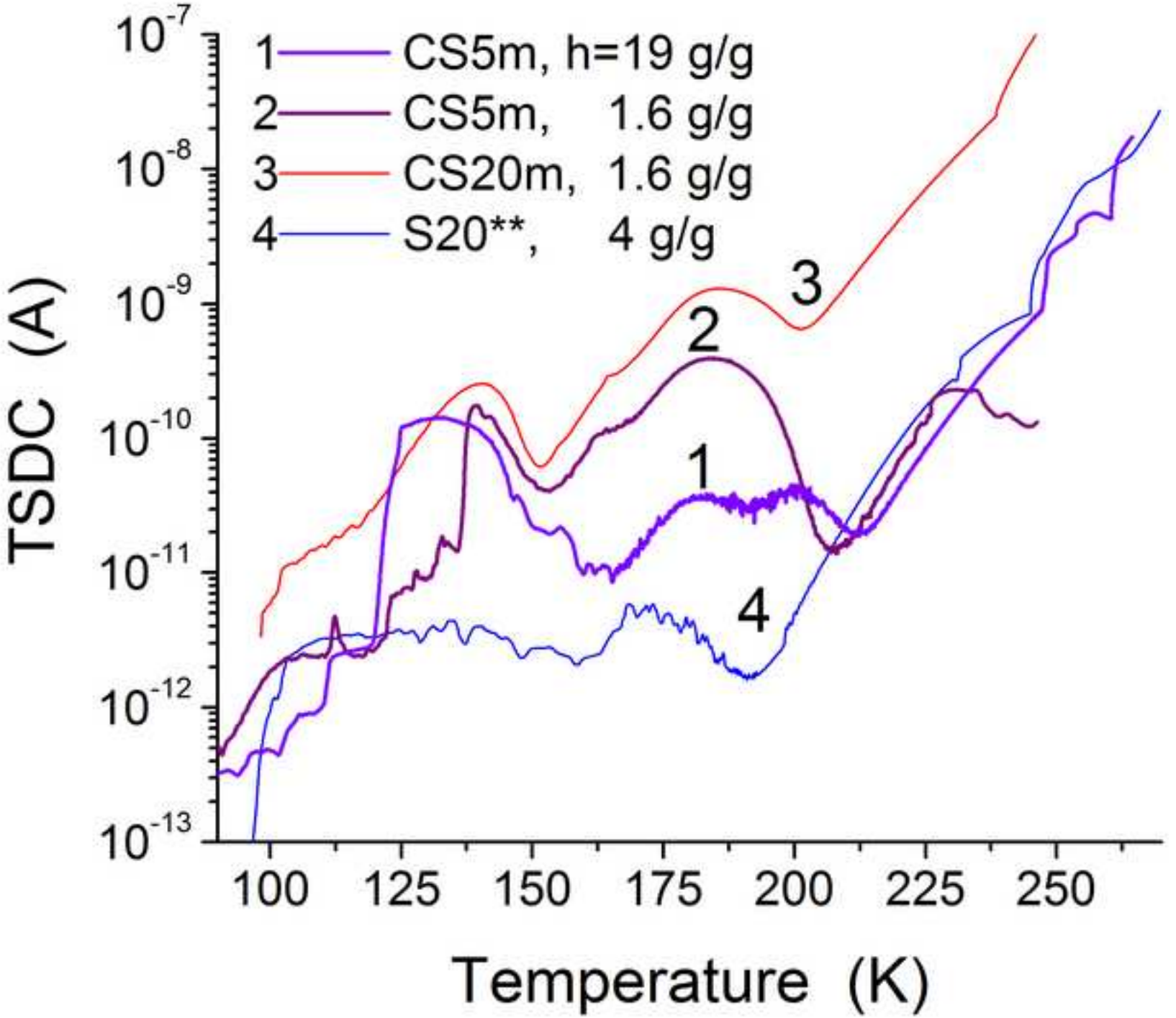
1 CS5m, h=19 g/g
2 CS5m, 1.6 g/g
3 CS20m, 1.6 g/g
4 S20**, 4 g/g
TSDC (A)
Temperature (K)
10-7
10-8
10-9
10-10
10-11
10-12
10-13
100
125
150
175
200
225
250
1
2
3
4

Figrure 13